ACS OMEGA

http://pubs.acs.org/journal/acsodf

Article

Theoretical FRET Efficiency of an Antenna Material Containing Natural Dyes and Zeolite L

Jesús Francisco Monzón-Bensojo,* Manuel Alberto Flores-Hidalgo, Ruth Flores-Barraza, and Diana Barraza-Jiménez

Cite This: *ACS Omega* 2023, 8, 15594−15610

Read Online

ACCESS | Metrics & More | Article Recommendations | Supporting Information

ABSTRACT: We calculated the Förster resonance energy-transfer (FRET) efficiency of a theoretical host−guest composite formed by all-*trans* β-cryptoxanthin (BCRY), all-*trans* zeaxanthin (ZEA), and a zeolite-LTL (Linde Type L) nanochannel with the help of computational chemistry tools. Climate change demands urgently the development of novel renewable energies, and in such a context, artificial photosynthesis arises as a promising technology capable of contributing to satisfying humankind's energy needs. All artificial photosynthetic devices need antennas to harvest and transfer energy to a reaction center efficiently. Antenna materials integrated by highly fluorescent synthetic pigments embedded onto the nanochannels of a zeolite-LTL have already been shown experimentally to be very efficient supramolecular assemblies. However, research work computing the efficiency of an antenna made of nonfluorescent natural pigments and a zeolite-LTL nanochannel has not been undertaken yet, at least to our knowledge. Fortunately, natural dyes possess outstanding features to study them dynamically; they are environmentally friendly, inexpensive, ubiquitous, and abundant. Density functional theory (DFT) methods were chiefly employed along with the CAM-B3LYP functional and the 3-21G*/6-311+G(d,p) basis sets. The ONIOM method enabled geometry and energy calculations of dyes inside the zeolite-LTL (ZL) nanochannel. The Förster resonance energy-transfer (FRET) efficiency and the Förster radius of the composite were 40.9% and 24.9 Å, respectively. Theoretical findings suggested that this composite might contribute to diminishing costs and improving the environmental friendliness of an antenna system.

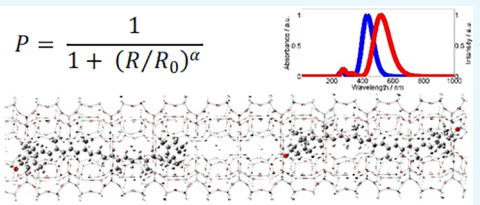

INTRODUCTION

Humankind depends on electricity, heating, cooling, and transportation to satisfy its daily-life needs. Regrettably, more than 75% of the required energy for such purposes comes from fossil fuels, resulting in the increase of greenhouse gases in the atmosphere, which leads in turn to climate change.[1] Development of renewable energies such as solar, geothermal, wind, biomass, and hydropower has contributed successfully to mitigating climate change, being solar energy a resource that stands out from the rest because of its availability throughout the earth's surface.[2]

Silicon-based technology remains dominant on the market, exhibiting panel efficiencies of more than 21% and stabilities superior to 25 years, becoming currently the cheapest option for electricity production. However, this photovoltaic industry needs to avoid its dependence on subsidies and see further improvement of its economic parameters.[3] In the case of pigments of dye-sensitized solar cells (DSSCs), they suffer from considerable photodegradation, requiring novel solutions to increase the lifetime of the cells.[4] On the other hand, artificial photosynthesis emerged as a scientific discipline intended for obtaining useful energy for humankind, such as electricity. The first step in any artificial photosynthetic device is an antenna system to harvest and transfer solar energy via Förster resonance energy transfer (FRET) to a reaction center efficiently.[5,6]

During the beginning of the 21st century, ZL crystals became a very attractive host system to assess energy-transfer mechanisms. All ZL nanochannels present in crystals are parallel to each other, and they have the same pore diameter of 7.1 Å; the one-dimensionality of nanochannels confers them an optical anisotropy, where FRET among guest dyes is extremely fast. A crystal bearing a diameter of 600 nm possesses around 100,000 nanochannels; thus, a 60 nm × 60 nm (diameter and length) crystal is able to host nearly 40,000 molecules if they have a length of 1.5 nm.[7] ZL might be the only known material with a thermal and mechanic stability that has linear channels of about 1 nm diameter.[8]

Dyes inside nanochannels exhibit unusual photophysical and photochemical properties due to the confinement offered by the host system. This confinement protects molecules from undesirable reactions such as photodegradation, oxidation, and

Received: February 15, 2023
Accepted: April 4, 2023
Published: April 19, 2023

photoisomerization.[9] Crystals can lie perpendicularly on a glass substrate to build monolayers, increasing their optical anisotropy and sunlight harvesting area; monolayers can resist sonication.[10] Theoretical studies of synthetic pigments within nanochannels have computed FRET efficiencies near unity, showing energy-transfer steps 150 times faster than any natural antenna.[11]

Even very photolabile dyes in solution remain without significant photodegradation once they enter ZL nanochannels.[12] Ionic dyes in solution adsorb themselves onto nanochannel walls through ion-exchange mechanisms, while neutral dyes require an insertion in the gas phase or from dispersions.[8]

Molecules inside ZL nanochannels at high loadings (20%) undergo Davydov excitonic J-coupling, leading to the appearance of linear J-aggregates at both ends of nanochannels, while dyes between the ends of nanochannels do not form these aggregates.[13,14] Therefore, both Förster and Davydov energy-transfer mechanisms coexist in the same antenna material, and molecular spacers control end-to-end intermolecular distances to employ simultaneously both mechanisms to increase energy transfer.[15] J-aggregates emit at longer wavelengths and decay faster than isolated monomers so that J-aggregates can replace a traditional acceptor in an antenna system.[16] As donors and acceptors can bear identical chromophores, it is easier to choose a dye to span a target absorption bandwidth, where both pigments contribute to absorbing the suitable photons with the same efficiency. While the Calzaferri group patented the first photonic antenna material based on ZL called ZeoFRET,[17] Calzaferri published by himself an essential book chapter that summarizes the state-of-the-art of dye−ZL composites.[8]

Computational-experimental combined studies have become indispensable resources to elucidate the relationship between detailed structural information of dye−ZL composites and their optical properties.[8] The groups of Fois[18−24] and Insuwan[25−27] have published excellent high-level combined investigations on dye−ZL composites. The ONIOM method has guided theoreticians to acquire accurate results at a low computational cost, modeling host systems with a low level of theory such as molecular mechanics (MMs) and simulating guests with a higher level of theory such as the density functional theory (DFT).[28]

Nevertheless, the employment of synthetic materials usually presents inherent drawbacks. They may contain an identified pollutant, e.g., the photovoltaic device with the current highest efficiency (47.1 ± 1.6%) has five out of six cells containing arsenic.[29] They may also require endangered, scarce elements (e.g., gallium, indium, and ruthenium) not available in the medium term.[30] Multistep synthesis procedures often involve a variety of solvents and time-consuming purification processes, which may make synthetic dye production expensive in spite of the development of novel pigments.[31] Conversely, natural dyes are completely environmentally friendly due to their natural occurrence, and they are both abundant and ubiquitous.[32]

Finally, oxygenated carotenoids such as all-*trans* β-cryptoxanthin and all-*trans* zeaxanthin in methanol peak strongly about 450 nm; both xanthophylls are among natural and synthetic dyes with the highest molar absorptivity values ε = 139,400 and 138,800 M^{-1} cm^{-1} in methanol, respectively. Optical properties of carotenoids derive from the extent of their polyene structure. Carotenoids absorb strongly in the visible spectrum, but their fluorescence quantum yields in solution are quite low. The electronic transition ($S_1 \rightarrow S_0$) between the first excited state ($2^1A_g^-$) of carotenoids and their ground state ($1^1A_g^-$) is symmetry-forbidden, while that of their second excited state ($1^1B_u^+$) is symmetry-allowed ($S_2 \rightarrow S_0$). Fast conformational changes experienced by carotenoids in solution also favor the exchange between *cis* and *trans* configurations along with other molecular distortions. These molecular deformations cease once dyes enter ZLCHs; a plethora of synthetic pigments have shown their adherence to such a behavior.[8,33−35]

The main aim of this work was computing the FRET efficiency of a dimer embedded onto a ZL nanochannel (ZLCH) and evaluating the overall effect in the FRET efficiency under unfavorable conditions such as long dyes with extremely low fluorescence quantum yields and under favorable conditions such as one-dimensionality and optical anisotropy of the host system. We carried out computations of the monomers in methanol to compare results between the anisotropic and isotropic mediums.

COMPUTATIONAL CALCULATIONS

Consistently, computations were performed with the help of Gaussian 16 software unless another software is mentioned, and they were run in the gas phase with the exception of those calculated for monomers in methanol.[36] Geometrical considerations are based on space-filling arguments, and after each geometry optimization, a frequency calculation followed to discard imaginary frequencies. Interaction energies were counterpoised-corrected, while excitation energies were vertical and singlet.[37] While data needed to create absorption and emission spectra were obtained with the help of Gaussian software, spectral figures and computations of fluorescence quantum yields and spectral overlaps were attained with the help of ale software.[38] Geometry optimizations, ground-state energies, and absorption spectra of monomers in methanol were computed in our last work.[39]

Geometry Optimizations and Calculations of Ground-State Energies of Isolated Dimers. First, monomers adopting a horizontal and parallel position with respect to each other were accommodated in four identical isolated dimers with the help of Argus Lab Software, and then, monomers were separated arbitrarily at end-to-end intermolecular (IM) distances of 10, 14, 17, and 21 Å to find the isolated dimer with the lowest interaction energy.[40] Isolated dimers' geometry optimizations were run with a CAM-B3LYP/3-21G* level of theory, adding a polarization function by hand.[41,42] CAM-B3LYP is a functional that employs 0.19 Hartree−Fock plus 0.81 Becke 1988 exchange interaction in the short range and 0.65 HF plus 0.35 B88 in the long range. It uses the Lee−Yang−Parr correlation and the correlation functional 0.19 VWN5 + 0.81 LYP. CAM-B3LYP has reproduced satisfactorily experimental UV−vis electronic transitions ($\pi \rightarrow \pi^*$) of large organic dyes with delocalized excited states.[43] Furthermore, computed geometrical parameters of ZEA were in good agreement with those reported for the crystalline structure,[44] showing that the CAM-B3LYP/3-21G* level of theory can attain reasonable geometries of large systems.[45−50] Geometrical parameters such as the final end-to-end IM distance between monomers, monomers' coplanarity loss, and monomers' atom-to-atom intramolecular (iM) distortions come from ground-state geometry optimizations. Isolated dimers' ground-state energies were achieved with a CAM-B3LYP/6-311+G(d,p) level of theory; the last basis set

https://doi.org/10.1021/acsomega.3c01010
ACS Omega 2023, 8, 15594−15610

of triple-ζ quality is widely employed to obtain accurate molecular energies.[51]

Excited-State Geometry Optimizations and Emission Spectra of Monomers in Methanol. Geometry optimizations were run from excitation energies of absorption spectra employing a CAM-B3LYP/6-311+G(d,p) level of theory. Ten excited states were calculated from the latter geometries with the help of the TDA−DFT-CAM-B3LYP/6-311+G(d,p) method.[52,53] The Tamm Dancoff approximation (TDA) along with TDDFT allows computations of UV−vis spectra of large molecules within 500−1000 atoms; test sets obtained mean absolute deviations (MADs) in the range of 0.2−0.3 eV. The polarizable continuum solvation model was employed because it uses a molecular cavity following the real geometry of the investigated system and it makes use of a surface charge distribution to represent the polarization of the environment.[54] Emission spectra of monomers in methanol were derived from the last excitation energies.

Building of the Zeolite-LTL Nanochannel. A zeolite framework identified with an LTL code was downloaded from the Database of Zeolite Structures.[55] The framework consisted of three unit cells and crystallographic parameters of $a = b =$ 18.40 Å and $c = 7.52$ Å. Atoms beyond those surrounding the ZLCH were removed, yielding a smaller, modified nanochannel. As the Si/Al ratio in the nanochannel was 3:1, a suitable number of cations (K^+ and Na^+) was placed inside the modified nanochannel to compensate for the negative charge of the $(AlO_2)^{-1}$ unit. The modified-nanochannel geometry optimization was carried out with an MM/UFF level of theory; all atoms were fully relaxed during the optimization.[56,57] Eventually, 17 unit cells were added to the three-unit-cell modified nanochannel with the help of Avogadro software to obtain the definitive 20-unit-cell nanochannel that hosted dimers or monomers during this study; the narrower free diameter of the ZLCH was 7.1 Å.[58]

Calculation of Optimized Geometries and Ground-State Energies of Complete Composites. Each of the aforementioned four optimized isolated dimers was inserted into a ZLCH with the help of Argus Lab software. Geometry optimizations of complete composites were achieved with the ONIOM:DFT/CAM-B3LYP/3-21G*:MM(UFF) method, while ground-state energies were accomplished replacing 3-21G* by the 6-311+G(d,p) basis set. Dimers were the high layer, while the ZLCH served as the low layer. All atoms of the ZLCH were kept frozen at their crystallographic positions, whereas all atoms of dimers were allowed to fully relax. Others have modeled dyes inside a ZLCH with methods similar to those employed herein.[18−27]

Excited-State Geometry Optimizations and Absorption and Emission Spectra of Individual Composites. We created two so-called individual composites (ICs), with each IC consisting of a whole ZLCH and only one monomer. The methodology to compute geometry optimizations and ground-state energies of ICs was the same as that of the complete composites. Ten excited states of both ICs were calculated from their ground-state geometries with the use of the TDA−DFT/ONIOM/CAM-B3LYP/6-311+G(d,p):MM-(UFF) method. UV−vis absorption spectra of ICs were acquired from these excitation energies that were utilized in turn for calculating new geometries with a CIS/3-21G method. The configuration interaction single method usually obtains accurate excited-state geometries in investigations of large systems such as polycyclic aromatic molecules and thiophene and phenylene vinylene oligomers. The CIS/3-21G method is particularly useful in computing geometries of delocalized singlet excited states ($\pi \rightarrow \pi^*$) with a HOMO → LUMO character (L_a), yielding a good agreement with experiments.[59−61] Ten new excited states were computed from the latter excited-state geometries to derive the UV−vis emission spectra of each IC with the help of the TDA−DFT/ONIOM/CAM-B3LYP/6-311+G(d,p):MM(UFF) method. Ultimately, eqs S1−S3 explain how each value of spectral absorbance and intensity was acquired.

RESULTS AND DISCUSSION

Geometry and Energy of Isolated Dimers in the Ground State. DX refers to an isolated dimer *D* formed by a donor and an acceptor, whose end-to-end IM distance is X Armstrong. First, Table S1 shows a comparison between geometrical parameters of ZEA in all isolated dimers and those found in the X-ray crystalline structure in order to assess the ability of the 3-21G* basis set in describing the geometry of ZEA. RMSDs for bond lengths, bond angles, and dihedral angles were 0.012 Å, ≤1.6°, and ≤4.9°, respectively. These results are in line with the stereochemical standards employed during structure refinement of macromolecular residues such as peptides and nucleotides, where suggested RMSDs for bond lengths, bond angles, and dihedral angles are 0.010−0.020 Å, 0.5−2.0° and 2.0−4.0°, respectively.[62,63] It should be kept in mind that ZEA in the crystalline structure did not interact with another molecule as it did in the isolated dimer. Besides, isolated monomers had already undergone geometry optimizations with a B3P86/6-31G(d) level of theory in our last work, making geometry optimizations of isolated dimers even more accurate in this study.

As shown in Table S2, monomers in D10, D14, and D21 experienced final negligible end-to-end IM displacements along their *x*-Cartesian axis (<1%), indicating a good balance among electrostatic, exchange, induction, and dispersion interaction energies. In contrast, IM attraction forces predominated in D17, forcing monomers to reach an equilibrium at 15.385 Å, with an IM displacement of −12.81%, making D17 the most unstable isolated dimer.

CL of the polyene chain (PCH) stands for 180° − X°, where X° represents the value of any dihedral angle in degrees. As displayed in Tables S3 and S4, CL of both monomers in the four isolated dimers ranged from 0.17 to 0.25°, with a variance coefficient (VC) lower than 0.2%. The last results show that IM interactions and iM distortions of isolated dimers did not affect significantly the CL in any monomer. The photoactive region of each monomer spans the PCH and one conjugated double bond in each side ring (Figures S1a and S2a, drawn with the help of ChemBioDraw software).[64] Figures S1b−e and S2b−e confirm that the PCH of monomers stood straight in isolated dimers after geometry optimizations. Emissive molecules have highly coplanar photoactive regions, which in turn lead to a more efficient energy transfer.[65] Figure S3a shows the initial molecular alignment of isolated dimers along their *x*-Cartesian axis, while Figure S3b-e exhibits the final molecular alignment of isolated dimers. Unlike D17, the remaining isolated dimers preserved a good alignment along their *x*-Cartesian axis. The more aligned the monomers along their *x*-Cartesian axis, the more favorable the alignment of ETDMs inside ZLCHs and, consequently, the higher the FRET efficiency.[8]

https://doi.org/10.1021/acsomega.3c01010
ACS Omega 2023, 8, 15594−15610

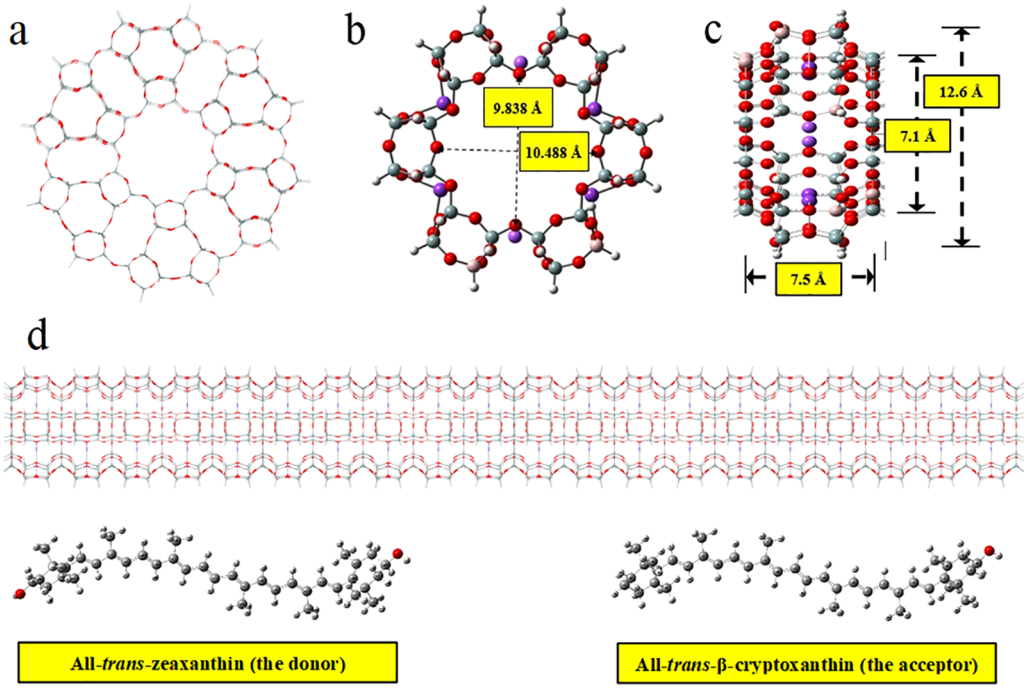

Figure 1. (a) Front view of a complete theoretical framework of a zeolite-LTL nanochannel. (b) Front view of the reduced zeolite-LTL nanochannel used in this study, showing oxygen-to-oxygen distances of O1−O1 and O2−O2 indicated by vertical and horizontal arrows, respectively. (c) Side view of a unit cell of a zeolite-LTL nanochannel showing the unit cell length and displaying both the narrower and wider diameters. (d) Side view of the 20-unit-cell definitive zeolite-LTL nanochannel. Zeaxanthin (donor) and β-cryptoxanthin (acceptor) appear above the nanochannel.

Assessment of atom-to-atom iM distortions of monomers in isolated dimers with respect to that of their counterparts in methanol was necessary for establishing quantitatively the degree of deformation of each monomer in the isolated dimer resulting from interaction energies (Table S4). After contrasting deviations of atom-to-atom iM distances of monomers with those shown by their counterparts in methanol, the total sums of deviations per molecule (TSDMs in Table S4) were 6.8 and 5.2 Å for BCRY and ZEA, respectively. This difference might be owing to the center-symmetric structure of ZEA, which would make it more resistant to atom-to-atom iM distortions. Table S4 also displays that isolated dimers with the least deformed monomers were D14 (2.1 Å) and D17 (2.5 Å). BCRY distorted itself chiefly along its *y*-axis (5.5 Å), whereas the ZEA main deformation took place along both its *z*-axis (3.0 Å) and its *y*-axis (1.4 Å). Distortions along *y*- or *z*-axes might be experimentally desirable for dimers entering a ZLCH because there would be a higher probability that monomers' surfaces reached an adsorption site onto inner walls. Unlike BCRY in D10 and ZEA in D21, atom-to-atom iM deformations of BCRY and ZEA in isolated dimers were ≤1.4 and ≤1.2 Å, respectively.

On the other hand, the interaction energy (IE) is the contribution to the total energy caused by an interaction between monomers, which usually depends on their relative position. Physically distinct contributions dominate the IE of two monomers in the vacuum: electrostatic, exchange, induction, and dispersion energies. The supramolecular approach is the most straightforward way for calculating IEs, and it takes into account exclusively the difference between the energy of the dimers and all of their isolated energies.[66,67]

$$DY_{IE}^{cp} = DY_E(DA) - D_E(DA) - A_E(DA) \quad (1)$$

where DY_{IE}^{cp} is the counterpoised (cp) IE of the isolated dimer, $DY_E(DA)$ is the energy of the isolated dimer, $D_E(DA)$ is the energy of the donor calculated in the isolated dimer DA, and $A_E(DA)$ is the energy of the acceptor calculated in the isolated dimer DA.

Although DFT is not suitable for computing IEs because functionals should be nonlocal as the dispersion energy, electronic structure methods such as the symmetry-adapted perturbation theory based on DFT (SAPT (DFT)), MP2, and CCSD (T) are computationally expensive and limited to dimers of small organic molecules containing as many as 30 atoms. In addition, the use of finite basis sets smaller than aug-cc-pVTZ increases the basis set superposition error (BSSE), which artificially enhances the binding in a dimer.[67]

The goal of computing IEs of isolated dimers was to identify the isolated dimer with the lowest IE in order to model the selected isolated dimer in the ZLCH irrespective of whether the IEs were suitable for a benchmarked data set or not. The lowest IE indicates the most stable conformation for the donor and the acceptor in a neutral electronic state; the more negative the IE, the more probable it is to find the donor and acceptor at this geometrical conformation, displaying the highest stability.[68]

Eventually, as presented in Table S5, IEs of isolated dimers were virtually identical, once considering all significant figures to the right of the decimal point (12.296 eV). IEs only represented 0.4% of the total energy as expected from the supramolecular approach; the positive sign of the IEs indicates that the isolated dimers are less stable than the isolated monomers. As no IE was significantly lower than the others, we decided to again place each isolated dimer at approximate end-

https://doi.org/10.1021/acsomega.3c01010
ACS Omega 2023, 8, 15594−15610

to-end IM distances of 10, 14, 17, and 21 Å in a ZLCH for calculating FRET efficiencies in four composites (C10, C14, C17, and C21).

Stoichiometry and Structure of the Zeolite-LTL Nanochannel. The empirical formula of the definitive ZLCH was $K_{0.4}Na_{0.2}[(Al_{1.0}O_{1.6})\ (Si_{2.8}O_{4.7})]:H_{2.0}$, and it agreed with its experimental counterpart reported in the literature: $K_{0.75}Na_{0.25}[(Al_{1.0}O_{2.0})(Si_{3.0}O_{6.0})]$.[7] The sum of all atoms in the experimental empirical formula was 13.0, while it was 12.7 in the theoretical ZLCH. To avoid dumping bonds and to preserve the neutral nature of the ZLCH, hydrogen atoms replaced other atoms that would occur naturally at the limits of a complete framework of the ZLCH. Figure 1a shows a front view of the complete framework of a ZLCH, while Figure 1b displays a front view of the ZLCH employed in this study. Figure 1a also shows that oxygen-to-oxygen interatomic distances found here for O1−O1 (10.10 Å) and O2−O2 (10.43 Å) agreed with those computed by others (9.83 and 10.48 Å, respectively).[22] Figure 1c exhibits a side view of a unit cell of the ZLCH with a length of 7.5 Å, a narrower diameter of 7.1 Å, and a wider diameter of 12.6 Å, reproducing well the experimental parameters. Figure 1d displays a side view of the 20-unit-cell ZLCH utilized in this study to model dimers and monomers inside. In conclusion, the ZLCH should properly simulate the nanoenvironment prevailing within the inner walls of a physical ZL.

Geometry and Energy of Complete Composites in the Ground State. A complete composite consisted of an isolated dimer inside a ZLCH. As evidenced in Table S6, IM displacements of monomers in complete composites were higher than those experienced by isolated dimers. Exchange and repulsive-electrostatic IEs predominated in C14, C21, and C10, with IM displacements of +1.2, +6.2, and +31.5%, respectively. Interestingly, final end-to-end IM distances of monomers in D17 and C17 were almost identical, 15.385 and 15.337 Å, respectively. Attractive-electrostatic, induction, and dispersion IEs prevailed in C17, where the IM displacement was −7.1%. IM displacements were necessary to establish the distance R between ETDMs, which, along with the Förster radium of a dimer, would enable calculations of FRET efficiencies.

As shown in Tables S7 and S8, the PCH of both monomers presented CL values that oscillated from 4.00 to 5.98°, derived from the huge electric fields that prevail inside ZLCHs that range from several MV cm^{-1} up to GV cm^{-1}.[63] CLs of monomers in complete composites were almost 24 times higher than those of isolated dimers. The total CLs of the PCH of ZEA and BCRY in complete composites were 21.22 and 20.45°, respectively (Table S9), indicating that in the case of complete composites, the center-symmetric chemical structure of ZEA did not avoid a slightly higher CL to that of BCRY. The total CL for both monomers in C21, C14, C10, and C17 followed the next ascending order: 9.55, 9.62, 10.66, and 11.84°, respectively.

Other theoretical studies carried out in the gas phase determined the CL for certain synthetic pigments in solution and inside ZLCHs. For example, *trans*-azobenzene and Acriflavine hydrochloride in a K^{+1}-ZLCH presented CL values of 16.0 and 8.6°, respectively.[18,20] These synthetic pigments occupied less than two unit cells in the ZLCHs, whereas the natural dyes in the present study filled about four unit cells. Perhaps, this size difference would have prevented natural dyes from having the option of freely rotating, thus diminishing their CL.

As displayed in Table S10, ZEA suffered an additional atom-to-atom iM distortion of 5.3 Å after entering the ZLCH, while the additional atom-to-atom iM distortion of BCRY inside the ZLCH was 11.1 Å. Even though the center-symmetric chemical structure of ZEA did not avoid its CL from being slightly higher than that of BCRY, it seemed that its center-symmetric chemical structure would have helped resist atom-to-atom iM deformations in such a hostile nanoenvironment. On the contrary, the additional atom-to-atom iM deformation of BCRY within the ZLCH (11.1 Å) was 1.6-fold higher than that experienced by BCRY in isolated dimers. The additional atom-to-atom iM distortion suffered by BCRY was mainly along its *z*-axis (5.2 Å), while ZEA distorted itself chiefly along its *y*-axis (3.5 Å). Again, these kinds of deformations might be suitable experimentally to approach monomers to ZLNCH's inner walls, improving the eventual molecular adsorption. Monomers exhibited a much lower additional atom-to-atom iM distortion in C14 (2.7 Å) than in the remaining complete composites. Then, the high length of the monomers along with the relatively small magnitude of their IM and iM deformations (due to the ZLCH confinement) prevented them from lying perpendicularly inside a single unit cell, like happened with pyronine, oxonine, and methylacridine.[23,24]

Figures S4−S6 show the optimized geometries of dimers and monomers embedded onto ZLCHs, highlighting how the PCH approached, to a lesser or greater degree, the ZLCH's walls. In the case of C17 (the composite with the lower IE), the donor's oxygen atoms approached the ZLCH's wall pointing toward opposite directions, suggesting that there might be a strong ion−dipole interaction between extraframework cations and the hydroxyl groups. The donor's polyene backbone presented a sigmoid-like shape, and a few atoms in the middle also approached the wall, indicating that in the absence of a hydrogen-bond-forming coguest (like some solvent molecules), hydrogen bonds between oxygen atoms of the framework and the donor's hydrogen atoms might also be present. As the C17 acceptor has just one oxygen atom, the molecule exhibited a curved shape and even the lone oxygen atom remained close to the ZLCH's *c*-axis. It seemed that either there were no interactions between extraframework cations and the lone oxygen atom or this interaction is much weaker than that of the right-sided oxygen atom of the donor. As the acceptor's polyene backbone also approached the ZLCH's wall, some hydrogen bonds could be part of this structural behavior. Hydrophobic interactions might be present as both monomers are very nonpolar compounds.

Very strong and weaker interactions in dye−ZL composites are never a trivial issue, and these interactions can change the structural and optical properties of the pigments, which leads in turn to a variety of fine-tuned technological devices.[8] For instance, a fluorenone-ZL composite showed an impressive stability under GPa pressures; achievement of such stability involved the pressure-strengthening of interactions between dyes' carbonyl oxygens and ZL K^+ cations.[18] Likewise, based on space-filling arguments, some perylene diimide dyes should not enter ZLCHs because the size of the pigments exceeds the pore diameter of the ZLCHs (7.1 Å). However, the energetic force that drove the slip and transit of a molecule along ZLCHs was a strong interaction between two out of four carbonyl oxygens of the dye and two ZL K^+ cations.[19,20] In our last work, we discarded all-*trans*-lutein and all-*trans*-neoxanthin

https://doi.org/10.1021/acsomega.3c01010
ACS Omega 2023, 8, 15594−15610

because their y-axes lengths were 7.3 and 7.2 Å, respectively. The slip and transit of perylene along the ZLCHs make us believe that this behavior might repeat experimentally with our rejected dyes.

Also, stopcock molecules' heads irreversibly modified ZLNCHs' entrances by condensing with OH groups; small-tail-groups' stopcocks resembled opened lids, and their full closure required a double condensation. Bulky-tail-groups' stopcocks sealed the entrance like a cork. Hydrogen bonding from coadsorbed water played a major role in the stopcock-ZL stability.[21] Strong dye−ZL interactions, dye−dye van der Waals interactions, and hydrogen bonds from coadsorbed water were responsible for the invention of the first quasi-one-dimensional (1D) supramolecular nano ladders built with maximally packed fluorenone molecules inside ZLCHs.[22]

On the other hand, the calculation of IEs of complete composites had to take into account the resulting deformation energies of monomers, derived from the interplay between flexible molecules and the host system.[66] Thus, eqs 2−4 lead to obtaining the desired IEs in the context of the supramolecular approach

$$C_{IE}^{cp} = C_E(DN) - DY_E(DN) - N_E(DN) - (Z_{\delta E} + B_{\delta E}) \quad (2)$$

where C_{IE}^{cp} is the counterpoised-corrected IE of the complete composite. $C_E(DN)$ is the ground-state energy of the complete composite. DN stands for a dimer D inside a ZLCH N. $DY_E(DN)$ is the ground-state energy of the dimer calculated without the ZLCH. $N_E(DN)$ is the ground-state energy of the ZLCH. $Z_{\delta E}$ is the deformation energy of ZEA inside the ZLCH, and $B_{\delta E}$ is the deformation energy of BCRY inside the ZLCH.

$$Z_{\delta E} = Z_E(N_{ZG}) - Z_E(IM_{ZG}) \quad (3)$$

$$B_{\delta E} = B_E(N_{BG}) - B_E(IM_{BG}) \quad (4)$$

where $Z_E(N_{ZG})$ is the ground-state energy of ZEA calculated from its ground-state geometry without the ZLCH. $B_E(N_{BG})$ is the ground-state energy of BCRY calculated from its ground-state geometry without the ZLCH. $Z_E(IM_{ZG})$ is the ground-state energy of ZEA calculated from the ground-state geometry of the isolated monomer in the dimer before entering the ZLCH, and $B_E(IM_{BG})$ is the ground-state energy of BCRY calculated from the ground-state geometry of the isolated monomer in the dimer before entering the ZLCH.

Table 1 indicates that the IEs of the complete composites were C17 (−9.344 eV) < C10 (−9.250 eV) < C21 (−9.238 eV) < C14 (−9.164 eV); IEs of complete composites were 13.4-fold higher than those of the isolated dimers. IEs fluctuated from −211.175 to −215.323 kcal mol^{-1}, resembling reasonably those computed by others for large systems. For instance, an interaction energy of −116 kcal mol^{-1} resulted from a streptavidin−biotin binding complex with 1,775 atoms, computed with an ab initio HF level and the 3-21G basis set.[69] Likewise, three stacked-like N-terminal sides of a helical peptide, with a molar mass of 963.768 g mol^{-1} at an average distance of 9.292 Å, gave an average interaction energy of −148.233 kcal mol^{-1}, employing a DFT formalism within the molecular fragmentation with the conjugate cap (MFCC) approach.[70]

Surprisingly, Table 1 also shows that although monomers in C14 presented the lowest IM displacement, CL, and atom-to-atom iM distortion, they showed the highest deformation energy (0.453 eV), whereas monomers in C17 that displayed the highest CL and atom-to-atom iM distortion showed the lowest deformation energy (0.397 eV), along with C21 (0.396 eV). The last behavior emphasizes the need for further research with QSAR techniques to find those critical geometrical variables that increase the FRET efficiency, besides reconciling them with energy information. The final FRET efficiency reported here for the composite was that of C17 because its lowest IE revealed that monomers in C17 would have the maximal stability among the four tested complete composites.

Table 1. Counterpoised-Corrected Interaction Energies of Complete Composites in eV

energy	C10	C14	C17	C21
C_{IE}^{cp}	−9.250	−9.164	−9.344	−9.238
C_{IE}^{cp} [kcal mol^{-1}]	−213.157	−211.175	−215.323	−212.880
C_E (DN)	−89,399.661	−89,399.482	−89,399.772	−89,399.668
DY_E (DN)	−90,894.593	−90,894.547	−90,894.601	−90,894.603
N_E (DN)	1,503.776	1,503.776	1,503.776	1,503.776
$Z_{\delta E}$	0.212	0.259	0.224	0.225
Z_E (N_{ZG})	−46,470.750	−46,470.704	−46,470.738	−46,470.738
Z_E (IM_{ZG})	−46,470.962	−46,470.963	−46,470.962	−46,470.962
$B_{\delta E}$	0.193	0.194	0.173	0.171
B_E (N_{BG})	−44,423.843	−44,423.844	−44,423.864	−44,423.865
B_E (IM_{BG})	−44,424.036	−44,424.037	−44,424.036	−44,424.036
$Z_{\delta E} + B_{\delta E}$	0.405	0.453	0.397	0.396

Photophysical Properties of Monomers in Individual Composites. Monomers in ICs and methanol shared an identical set of computations from here, in order to compare data in anisotropic and isotropic systems, highlighting how this information influenced quantitatively the FRET efficiency.

Crucially, the molar absorptivity (ε) of any pigment inside a ZLCH is equal to $3\varepsilon \cos\theta$, where θ is the angle between polarized light and the c-axis of a ZLCH, the value of θ is one when the polarized light runs parallel to the aforementioned axis. Hence, we multiplied by three the absorbance in the absorption spectra of monomers inside the ZLCH to employ the appropriate molar absorptivity spectrum, referring to the last spectrum as the "corrected spectrum" in this study.[71]

Figure S7a−d shows that spectra of monomers in methanol presented two kinds of bands, a large main band (B1) with an emission range within 400−800 nm and an absorption range from 400 to 600 nm and a small far-UV band (B2) whose range of both emission and absorption fell within 200−350 nm. Table S12 exhibits that $\lambda_{max(emi.)}$ of BCRY ($S_2 \rightarrow S_0$, $1_1Bu^+ \rightarrow 1_1A_g^-$) and $\lambda_{max(abs.)}$ of ZEA ($S_2 \leftarrow S_0$) in B1 were 558.79 and 489.88 nm, respectively. The dimer in methanol possessed a Stokes shift of 68.91 nm; it is a very important spectroscopic feature in energy transfer because the smaller the Stokes shift of a dimer, the higher the spectral overlapping.

$\lambda_{max(emi.)}$ of BCRY and $\lambda_{max(abs.)}$ of ZEA (donor and acceptor, respectively, in the case of methanol) in B1 displayed large dipole strengths for the first excited state of 92.791 and 77.089 D, respectively. The main electronic transition of the first excited state was HOMO−LUMO (L_a character), having oscillator strengths (f) of 0.685 for the fluorescence emission of BCRY and 0.678 for the absorption of ZEA; the latter oscillator strengths agreed with those reported experimentally for a pyrazoline derivative in different solvents (f falling within 0.48−0.74). $\lambda_{max(emi.)}$ of ZEA was in excellent agreement with

https://doi.org/10.1021/acsomega.3c01010
ACS Omega 2023, 8, 15594−15610

that obtained experimentally for card-pack aggregates in ethanol/water (1:9, v/v) (560 nm) and in THF at RT (556 nm); zeaxanthin exists as a monomer in methanol.[72−74]

B2 in carotenoids has recently drawn attention because its $\lambda_{max(abs.)}$ value is identical for all E/Z isomers of a specific carotenoid, while $\lambda_{max(abs.)}$ is different from that of E/Z isomers of other carotenoids, allowing their experimental identification.[75] Table S12 shows that $\lambda_{max(emi.)}$ of BCRY ($2_1Bu^+ \rightarrow 1_1A_g^-$) and $\lambda_{max(abs.)}$ of ZEA ($2_1Bu^+ \leftarrow 1_1A_g^-$) in B2 were 267.15 and 265.19 nm, respectively, with the Stokes shift being barely 1.96 nm. The $\lambda_{max(abs.)}$ of ZEA in B2 correlated well with that obtained experimentally for β-carotene (274 nm), which bears the same chromophore as that of ZEA.[75] $\lambda_{max(emi.)}$ of BCRY and $\lambda_{max(abs.)}$ of ZEA in B2 had smaller dipole strengths of 2.830 and 3.972 D for their respective excited states, while the main electronic transitions were HOMO−LUMO + 2 (L_b character); both transitions had oscillator strengths of 0.487 and 0.524, respectively. The ratios of the height between B2 and B1 peaks for the $S_2 \rightarrow S_0$ transition of BCRY and the $S_2 \leftarrow S_0$ transition of ZEA were 0.063 and 0.094, respectively. Tables S13−S16 display the excitation energies of the remaining excited states.

Table S17 shows the spectral bandwidth at half-height where monomers emit or absorb strongly. The B1 bandwidths of the $S_2 \rightarrow S_0$ and $S_2 \leftarrow S_0$ transitions were virtually identical for both monomers as expected for two molecules sharing an identical chromophore and a solvent. The former spanned 142 nm from 497 to 639 nm, while the latter covered 108 nm from 441 to 549 nm. In the case of B2, the bandwidths of the monomers were almost the same in both electronic transitions, 36 nm (falling within 250−286 nm) for $2_1Bu^+ \rightarrow 1_1A_g^-$ and 43 nm (falling within 247−290 nm) for $2_1Bu^+ \leftarrow 1_1A_g^-$.

Table S18 displays the spectral overlap for the dimers BCRY/ZEA and ZEA/BCRY in methanol, demonstrating that these values were closely similar in both complete spectra and B2. The B2 spectral overlap contributed 1.3% to the overall spectral overlapping, a small contribution, but not negligible.

On the other hand, Table 2 shows the spectral overlap for the dimers ZEA/BCRY and BCRY/ZEA in the ZLCH. In this case, the former dimer offered a significantly higher spectral overlap with respect to that of the latter dimer due to spectroscopic reasons, explained in this subsection later on. Spectral overlaps for biological dimers in solution usually oscillate from 2.4×10^{-18} to 4.9×10^{-12} M^{-1} cm^3.[76] Dimers of synthetic dyes such as [acridine hydrochloride·acriflavine hydrochloride] and [1,1′-diethyl-2,2′-cyanine iodide·acriflavine hydrochloride] have shown experimental spectral overlaps of 9.8×10^{-16} and 6.0×10^{-16} M^{-1} cm^3 inside K^{+1}-zeolite-LTL nanochannels, respectively.[25,26] The well-known synthetic-dye dimer [pyronine·oxonine] presented an experimental spectral overlap of 1.5×10^{-13} M^{-1} cm^3 in ZL.[77] Additionally, the use of stopcock molecules has dramatically augmented the spectral overlap of other dimers; e.g., [pyronine·BTRX] and [B493/503·oxonine] have impressive values of 3.0×10^{-10} and 1.5×10^{-10} M^{-1} cm^3 in zeolites LTL, respectively.[78] Therefore, the theoretical spectral overlap of 4.162×10^{-13} M^{-1} cm^3 for the dimer ZEA/BCRY was suitable enough to consider it in a FRET mechanism. The B2 spectral overlap in ZLCH contributed 4.3% to the overall spectral overlapping, highlighting the weight of B2 in the energy-transfer process.

Intriguingly, Figure 2a−f shows that besides electronic transitions in B1 and B2 appearing anteriorly in methanol, spectra of ZEA and BCRY in the ZLCH depicted a *cis*-like

Table 2. Spectral Overlap of Monomers in the Zeolite-LTL Nanochannel

dimer	J [M^{-1} cm^{-1} nm^4][a]	J [M^{-1} cm^3][a]	P [%][b]
	Complete Spectrum		
zeaxanthin/β-cryptoxanthin	4.146×10^{15}	4.162×10^{-13}	100
β-cryptoxanthin/zeaxanthin	2.574×10^{15}	2.584×10^{-13}	100
	Far-UV Band		
zeaxanthin/β-cryptoxanthin	1.115×10^{14}	1.119×10^{-14}	4.3
β-cryptoxanthin/zeaxanthin	1.790×10^{14}	1.797×10^{-14}	4.3

[a]Spectral overlap in the most used units. [b]Contribution of the B2 spectral overlap to the overall spectral overlapping.

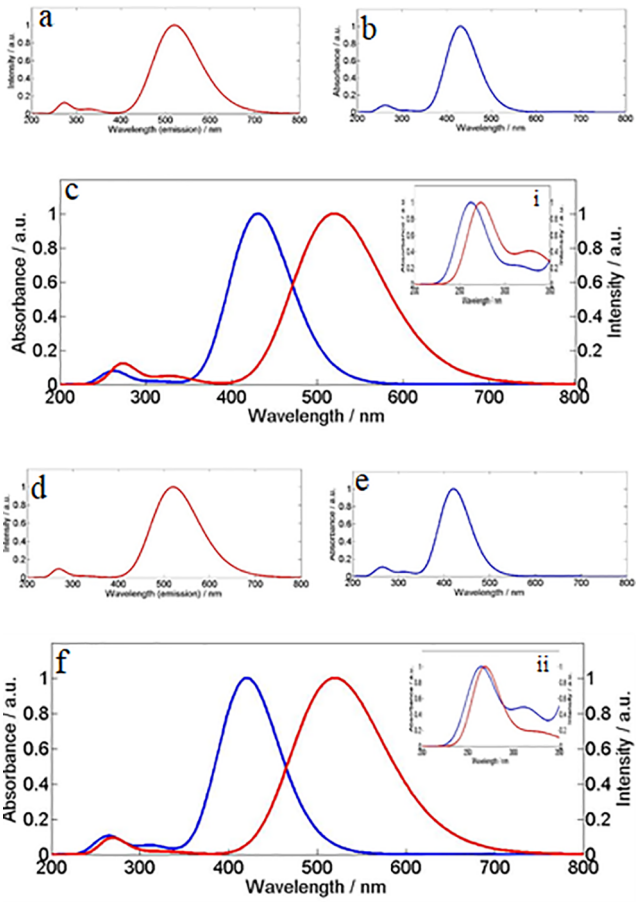

Figure 2. (a) Emission spectrum of zeaxanthin in the zeolite-LTL nanochannel (red line). (b) Absorption spectrum of β-cryptoxanthin in the zeolite-LTL nanochannel (blue line). (c) Complete spectral overlap between the normalized emission spectrum of zeaxanthin and the absorption spectrum of β-cryptoxanthin in the zeolite-LTL nanochannel. (ii) B2 spectral overlap between the normalized emission spectrum of zeaxanthin and the absorption spectrum of β-cryptoxanthin in the zeolite-LTL nanochannel. (d) Emission spectrum of β-cryptoxanthin in the zeolite-LTL nanochannel (red line). (e) Absorption spectrum of zeaxanthin in the zeolite-LTL nanochannel (blue line). (f) Spectral overlap between the normalized emission spectrum of β-cryptoxanthin and the absorption spectrum of zeaxanthin in the zeolite-LTL nanochannel. (iii) B2 spectral overlap between the normalized emission spectrum of β-cryptoxanthin and the absorption spectrum of zeaxanthin in the zeolite-LTL nanochannel.

https://doi.org/10.1021/acsomega.3c01010
ACS Omega 2023, 8, 15594−15610

Table 3. Excitation Energies Responsible for λ_{max} of the Bands in the Emission and Absorption Spectra of Monomers in the Zeolite-LTL Nanochannel

spectra[a]	n[b]	eV[c]	nm[d]	f[e]	μ^2 [D][f]	assignation of orbitals[g]	f[h]
				Main Band			
ZE	1	2.386	519.68	3.810	65.189	HOMO → LUMO	0.691
BA	1	2.878	430.81	4.087	57.969	HOMO → LUMO	0.677
BE	1	2.386	519.57	4.093	70.009	HOMO → LUMO	0.692
ZA	1	2.950	420.33	3.788	52.414	HOMO → LUMO	0.674
				Far-UV Band			
ZE	6	4.572	271.21	0.254	2.272	HOMO → LUMO + 2	0.432
BA	4	4.585	270.41	0.192	1.706	HOMO − 2 → LUMO	0.585
BE	6	4.634	267.56	0.340	2.998	HOMO → LUMO + 3	0.517
ZA	4	4.599	269.58	0.284	2.524	HOMO − 2 → LUMO	0.570
				cis-like Region			
ZE	3	3.776	328.33	0.163	1.766	HOMO → LUMO + 1	0.642
BA	2	3.901	317.81	0.063	0.657	HOMO − 1 → LUMO	0.617
BE	3	3.800	326.26	0.060	0.643	HOMO → LUMO + 1	0.637
ZA	2	3.938	314.82	0.180	1.862	HOMO − 1 → LUMO	0.586

[a]Kind of spectrum where the first letter stands for β-cryptoxanthin (B) or zeaxanthin (Z) and the second one indicates emission (E) or absorption (A). [b]Number of the excited state. [c]Excitation energy in eV. [d]Excitation energy in nm. [e]Oscillator strength of the excited state. [f]Dipole strength of the excited state in Debye. [g]Assignment of frontier molecular orbitals involved in the main electronic transition of the excited state. [h]Oscillator strength of the main electronic transition of the excited state.

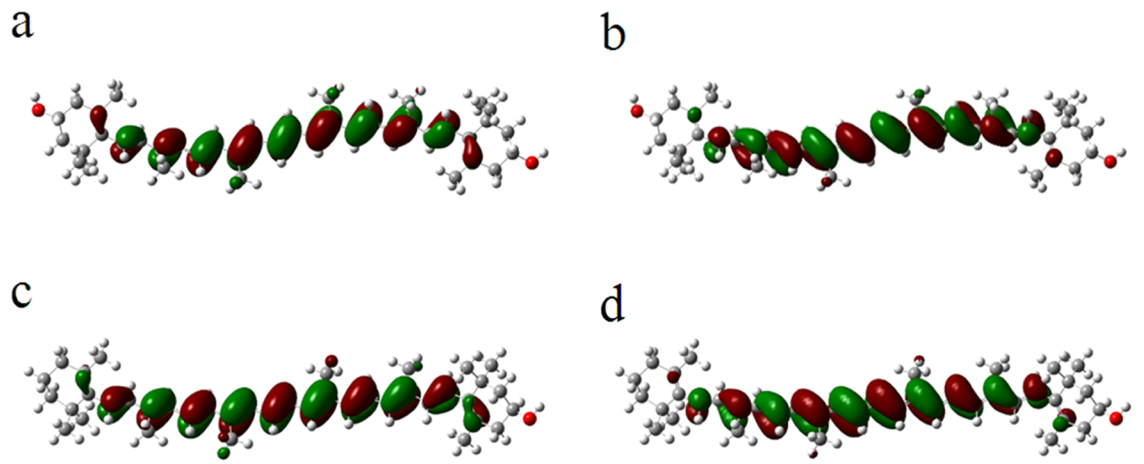

Figure 3. (a) Surface of HOMO of zeaxanthin in the emission spectrum of the individual composite. (b) Surface of LUMO of zeaxanthin in the emission spectrum of the individual composite. (c) Surface of HOMO of β-cryptoxanthin in the absorption spectrum of the individual composite. (d) Surface of LUMO of β-cryptoxanthin in the absorption spectrum of the individual composite.

region at the right of B2 within 300−350 nm (B3, shown by insets i and ii in Figure 2).

As initial monomers were full all-*trans*-isomers, there would not be any electronic transition there. The electronic transition responsible for a *cis*-peak in the absorption spectrum of carotenoids is $1_1Ag^+ \leftarrow 1_1A_g^-$. As shown in Table 3, this transition corresponds to $\lambda_{max(abs.)}$ of 314.82 and 317.81 nm for ZEA and BCRY, respectively. $\lambda_{max(abs.)}$ for ZEA experienced a hypsochromic shift of 17.19 nm with respect to that observed for ZEA in THF at RT (335 nm).[35] The involved frontier molecular orbitals in the main electronic transition of B3 were LUMO ← HOMO − 1 (L_b character), showing oscillator strengths of 0.586 and 0.617 for ZEA and BCRY, respectively. The values of f for the full second excited state where B3 emerged were 0.180 and 0.063, while the dipole strengths were 1.862 and 0.657 D for ZEA and BCRY, respectively. Oscillator and dipole strengths for the second excited state of monomers (B3) were lower than those observed in B1 and B2, but these *cis*-like regions would be yet capable of harvesting some high-energy photons.

The Q-ratio deals with the relationship between the height of a cis-peak and a main peak in an absorption spectrum; experimental Q-ratios for 9-cis, 13-cis, and 15-cis full isomers of zeaxanthin are 0.11, 0.43, and 0.48, respectively.[79] The Q-ratio of ZEA derived from Table 2 is 0.04.

As exhibited in Table S19, the ZEA presented an average CL > 10° in the following dihedral angles in the ground and excited states: C9−C10−C11−C12, C11−C12−C13−C14, and C13−C14−C15−C15′. Experimental Q-ratios for 9-*cis* and 13-*cis* full isomers of β-cryptoxanthin are 0.10 and 0.25, respectively.[79] The Q-ratio of BCRY derived from Table 2 is 0.01. Table S20 shows that unlike ZEA the average CL of BCRY oscillated from 0.98 to 5.70° in all dihedral angles in the ground and excited states. Although monomers did not undergo any full *cis* isomerization, the huge electric fields prevailing inside the ZLCH distorted monomers enough to force the appearance of a *cis*-like region in their absorption

https://doi.org/10.1021/acsomega.3c01010
ACS Omega 2023, 8, 15594−15610

Table 4. Integrated Fluorescence Intensity and Integrated Absorbance of Spectra of Monomers in the Zeolite-LTL Nanochannel

monomer[a]	spectra[b]	integral [nm^2][c]	A [%][d]	A [%][e]	integral [nm^2][f]	A [%][g]	A [%][h]	C [%][i]
				Dimer ZEA/BCRY				
Z	E	18,730,155.0	58.1	31.6	930,449.5	61.4	34.8	5.0
B	A	13,507,941.0	41.9		584,843.0	38.6		4.3
B	A_C	40,523,815.0		68.4	1,744,784.0		65.2	
total[j]		32,238,096.0	100.0		1,515,292.5	100.0		9.3
total[k]		59,253,970.0		100.0	2,675,233.5		100.0	
				Dimer BCRY/ZEA				
B	E	19,674,787.5	61.6	34.8	632,461.5	41.1	18.9	3.2
Z	A	12,278,598.0	38.4		906,598.5	58.9		7.4
Z	A_C	36,835,830.0		65.2	2,719,804.0		81.1	
total[j]		31,953,385.5	100.0		1,539,060.0	100.0		10.6
total[k]		56,510,617.5		100.0	3,352,265.5		100.0	

[a]Kind of monomer, zeaxanthin (Z) or β-cryptoxanthin (B). [b]Kind of spectrum, emission (E), absorption (A), or corrected absorption (A_C). [c]Integrated fluorescence intensity or integrated absorbance of the complete spectrum. [d]Integral of each spectrum in the total integral of the dimer as a percentage. [e]Integral of each spectrum in the total integral of the dimer as a percentage, utilizing the corrected absorption spectrum. [f]Integrated fluorescence intensity or integrated absorbance of the far-UV band. [g]Integral of each spectrum in the total integral of the dimer as a percentage. [h]Integral of each spectrum in the total integral of the dimer as a percentage, utilizing the corrected absorption spectrum. [i]Contribution of integrals of the far-UV band to that of the complete spectrum. [j]Sums made only with the normal absorption spectrum. [k]Sums made only with the corrected absorption spectrum.

spectra. Electric fields inside zeolites can reach from 64 MV cm^{-1} to 16 GV cm^{-1}, equivalent to 6.4−160 V in 80 Å, similar to the length of the ZLCH utilized to accommodate the monomers in this work.[80,81]

Figure 2 also shows that the emission range in B1 reduced itself from 400 nm in methanol to 300 nm in the ZLCH, whereas the absorption range in B1 remained at 200 nm. The range of emission fell within 400−700 nm, while that of absorption fluctuated from 350 to 550 nm, and the emission and absorption ranges of B2 stayed within 200−350 nm. Table 2 exhibits that $\lambda_{max(emi.)}$ of ZEA and $\lambda_{max(abs.)}$ of BCRY in B1 were 519.68 and 430.81 nm, respectively. The Stokes shift of the dimer in the ZLCH was 88.87 nm, surpassing that of its methanol counterpart by 19.96 nm. This is the reason why the spectral overlap in methanol was higher than that shown by the dimer embedded onto the ZLCH even after multiplying by three the absorption spectrum of BCRY in the ZLCH. Dipole strengths for the first excited state of $\lambda_{max(emi.)}$ of ZEA and $\lambda_{max(abs.)}$ of BCRY were still large (65.189 and 57.969 D, respectively), even though they were smaller than those displayed by the dimer in methanol. The main electronic transition of the first excited state was HOMO−LUMO too, having oscillator strengths of 0.671 for the $S_2 \rightarrow S_0$ electronic transition of ZEA and 0.697 for the $S_2 \leftarrow S_0$ electronic transition of BCRY; these oscillator strengths were almost identical to that of the dimer in methanol. The former and latter oscillator strength magnitudes showed a strong agreement with those reported for perylene diimide dyes (f = 0.76).[8] Tables S21−S24 contain the excitation energies of monomers in the ZLCH, not only for B1, B2, and B3 but also for the remaining excited states.

Figure 3 depicts the HOMO−LUMO surfaces of ZEA and BCRY in their $S_2 \rightarrow S_0$ and $S_2 \leftarrow S_0$ electronic transitions, respectively. HOMO surfaces covered all of the double bonds of the chemical structures, whereas LUMO surfaces appeared in eight central single bonds of the PCH; LUMO surfaces did not span fully the lateral C6−C7 and C6′−C7′ bonds; instead, the latter surfaces were present only in C7 and C7′ atoms.

$\lambda_{max(emi.)}$ of BCRY in the ZLCH underwent a hypsochromic shift of 39.22 nm with respect to that of its counterpart in methanol; this spectral behavior agreed with that of other synthetic pigments assessed experimentally in both a 0.2 M HCl solution and inside a K^{+1}-zeolite-LTL nanochannel. For instance, $\lambda_{max(emi.)}$ values of acridine hydrochloride and acriflavine hydrochloride were 540 and 469 nm, respectively, in solution, whereas $\lambda_{max(emi.)}$ decreased to 496 nm (a hypsochromic shift of 44 nm) and 438 nm (a hypsochromic shift of 31 nm) in the nanochannel, respectively. Further, the experimental $\lambda_{max(emi.)}$ of 1-[4-(4-dimethylamino-phenylethynyl)-phenyl]-2,2,2-trifluoro-ethanone in chloroform (592 nm) diminished to 546 nm once the pigment entered a K^{+1}-zeolite-LTL nanochannel (a hypsochromic shift of 46 nm).[26,27,82] Interestingly, $\lambda_{max(emi.)}$ of ZEA in the ZLCH was almost identical to that of the experimental S* state of zeaxanthin in THF at RT (520 nm). Although the latter state is often associated with molecular deformations like those experienced by ZEA in this study, the full spectral characterization of the S* state in carotenoids is still a matter of debate. Therefore, in order to state unambiguously that ZLCH nanoenvironment populated the S* electronic state of ZEA, further spectroscopic studies are necessary.[35,83]

Unlike the dimer in methanol, $\lambda_{max(abs.)}$ of ZEA (420.33 nm) was different from that of BCRY (430.81 nm), despite their chromophores sharing the same chemical structure. The measuring of CL and atom-to-atom iM deformations of monomers in solution and embedded onto ZLCHs may help to predict some of their optical properties. $\lambda_{max(abs.)}$ of BCRY and ZEA displayed huge hypsochromic shifts of 58 and 70 nm, respectively, with respect to those of their counterparts in methanol. To our knowledge, there are no theoretical or experimental reports of this photophysical behavior for other monomers in ZLCHs. The energies of $\lambda_{max(abs.)}$ of BCRY and ZEA were 2.950 and 2.878 eV, respectively. The former energy resembles closely that of lycopene (n = 11) in the following electronic, vibrational transition: $1^1B_u^+(v03') \leftarrow 1^1A_g^-(v00)$, which is 2.960 eV.[84] However, the latter energy is similar to that of a polyene (n = 11) in either of the next electronic,

https://doi.org/10.1021/acsomega.3c01010
ACS Omega 2023, 8, 15594−15610

vibrational transitions, $3^1A_g^-(v00') \leftarrow 1^1A_g^-(v00)$ or $1^1B_u^+(v00') \leftarrow 1^1A_g^-(v00)$, being 2.820 and 2.840 eV their respective values.[85] Further vibrational-resolved spectroscopic studies are necessary to elucidate the behavior of monomers in ZLCHs. The aforementioned hypsochromic shifts could be healthy for an antenna system because it would harvest higher-energy photons, delivering in turn more energy to an eventual reaction center and taking advantage of the solar radiation more efficiently, without leaving the region of the visible spectrum. The difference between $\lambda_{max(abs.)}$ of monomers in the ZLCH was responsible for the spectral overlap of ZEA/BCRY being higher than that of BCRY/ZEA.

Table S25 shows the integrated fluorescence intensity (EI) of emission spectra and the integrated absorbance (AI) of absorption spectra of both monomers in methanol. As expected for two monomers with identical chromophores and sharing the same solvent, EIs were closely similar (27,721,887 and 27,747,371 nm^2 for BCRY and ZEA, respectively), and likewise, AIs were closely similar too (20,513,643 and 20,511,092 nm^2 for ZEA and BCRY, respectively). EIs represented 57.5% of the total integral (TI, the sum of the integrals of the emission spectrum of the donor and the absorption spectrum of the acceptor), while AIs constituted 42.5% of the TI. On the contrary, AIs of B2 were 874,886 and 868,341.0 nm^2 for ZEA and BCRY, respectively, while those for emission bands were 605,160.5 and 601,392.5 nm^2 for BCRY and ZEA, respectively, representing AI 59.1% and EI 40.9% of the total integral. Note that B2 integrals contributed 6.5% to the TI of the complete spectra, highlighting that the presence of B2 in the spectra may be small, but it is not negligible whatsoever.

Table 4 contains EIs and AIs for full spectra and far-UV bands of monomers in ZLCHs. ZEA/BCRY/ZLCH exhibited a hyperchromic effect with respect to that of BCRY/ZEA/MeOH (≈22.8%). The total integral for the former composite was 59,253,970 nm^2, while it was 48,235,530 nm^2 for the latter system, using the corrected absorption spectrum for the dimer in the ZLCH. EIs for ZEA and BCRY were different from each other; irrespective of whether both monomers shared the same chemical structure of the chromophore, the same surrounding environment, and virtually identical values of $\lambda_{max(emi.)}$, EIs for the monomers were 18,730,155.0 and 19,674,787.5 nm^2, respectively.

The relationship between integrals of the monomers in the dimer where ZEA was the donor and BCRY was the acceptor changed from 58.1/41.9 to 31.6/68.4% after correcting the absorption spectrum. Corrected AIs of BCRY and ZEA were different from each other too, being 40,523,815.0 and 36,835,830.0 nm^2, respectively. Both monomers had the same chemical structure of the chromophore and the same surrounding environment. The bathochromic shift of $\lambda_{max(abs.)}$ of BCRY of 10.48 nm with respect to that of ZEA and the higher AI of the former monomer made the dimer ZEA/BCRY possess a larger spectral overlap than that of the dimer BCRY/ZEA. The increase of AI in B2 with respect to that of its counterpart in methanol was due to the occurrence of the *cis*-like region (B3) and the expansion of the AI due to the correction of the absorption spectrum. The total integral of B2 in the ZEA/BCRY dimer contributed 9.3% to that of the complete spectrum, becoming more relevant for the spectral overlap of the dimer than that shown by the BCRY/ZEA dimer in methanol.

Table 5 displays the spectral bandwidths at half-height of the monomers inside the ZLCH. The bandwidth of ZEA in the emission spectrum was 122 nm, encompassing a range of 466–588 nm, while the bandwidth for BCRY in the absorption spectrum was 84 nm, and it fluctuated between 393 and 477 nm. Despite both bandwidths being narrower than those shown by monomers in methanol, monomers in ZLCH would be able to harvest and transfer higher-energy photons. B2 bandwidths remained almost equal to that exhibited in methanol.

Table 5. Spectral Bandwidth at Half-Height of Monomers in the Zeolite-LTL Nanochannel

dimer[a]	bandwidth [nm][b]	lower limit [nm][c]	upper limit [nm][d]
	Main Band		
ZE	122	466	588
BA	84	393	477
BE	123	465	588
ZA	80	384	464
	Far-UV Band		
ZE	40	256	296
BA	39	245	284
BE	37	253	290
ZA	44	246	290

[a]The first letter indicates zeaxanthin (Z) or β-cryptoxanthin (B), and the second one represents emission (E) or absorption (A). [b]Bandwidth in nm. [c]Lower limit of the bandwidth. [d]Upper limit of the bandwidth.

FRET Efficiency of the Composite. A contribution of singlet–singlet Dexter energy transfer is very unlikely to occur as this mechanism is present at end-to-end IM distances ≤ 6 Å. The end-to-end IM distances of our monomers in any dimer (isolated or inside the ZLCH) were always higher than 9 Å. In fact, the end-to-end IM distance of C17 (the composite with the lower IE) was 15.337 Å, a distance that does not favor overlapping of molecular orbitals between monomers.[86,87]

In FRET, the donor–acceptor distance at which the FRET efficiency is 50%, *Ro*, is a function of the spectral overlap between the normalized emission spectrum of the donor and the absorption spectrum of the acceptor. If the measurement of the wavelength is in nanometers, then the critical distance is in Angstroms, given by

$$Ro = 0.211 \times \left[\frac{\kappa^2 \cdot \Phi_D \cdot J}{\eta^4}\right]^{1/6} \quad (5)$$

where κ^2 is the relative orientation factor between ETDMs of the donor and the acceptor, η is the refractive index of the environment, Φ_D is the fluorescence quantum yield of the donor in the absence of the acceptor, and J is the overlap integral. Here, J is in units of M^{-1} cm^{-1} nm^4.[65]

The fluorescence quantum yield of β-cryptoxanthin is not present in the literature, so it was necessary to compute it. Φ_D of a fluorophore can be obtained with the help of a reference compound of known Φ (Φ_{ref}); during the calculation of Φ_D, both molecules share the same excitation wavelength, gain, and slit bandwidths, obtaining then Φ_D with the equation

$$\Phi_D = \Phi_{ref} \times \frac{\eta^2}{\eta_{ref}^2} \times \frac{I}{A} \times \frac{A_{ref}}{I_{ref}} \quad (6)$$

https://doi.org/10.1021/acsomega.3c01010
ACS Omega 2023, 8, 15594−15610

Table 6. Fluorescence Quantum Yield of Zeaxanthin in the Zeolite-LTL Nanochannel

dye	λ_{exc} (nm)[b]	A (a.u.)[c]	I (a.u.)[d]	η	Φ_D
zeaxanthin	417	132,229	18,730,155	1[e]	1.662×10^{-4}
β-cryptoxanthin[a]	417	132,124	19,674,788	1[e]	1.747×10^{-4}

[a]The reference compound is β-cryptoxanthin, utilized as the sample in Table S16. [b]Excitation wavelength where the integrated absorbance of both monomers was as similar as possible. [c]Integrated absorbance taken from the spectra computed in the present study. [d]Integrated fluorescence intensity taken from the spectra computed in the present study. [e]Refractive index of vacuum.

Table 7. Magnitudes and Lengths of Excited- and Ground-State Dipole Moments of Monomers in the Zeolite-LTL Nanochannel

M[a]	x[b]	y[b]	z[b]	μ_{es}[c] [D]	x[d]	y[d]	z[d]	μ_{gs}[e] [D]	$\mu_{es} - \mu_{gs}$[f] [D]	l_{μ^*}[g] [Å]
Spectral Main Band										
Z	+7.198	−0.316	−0.708	7.240	−0.753	2.156	2.598	3.459	3.781	4.417
B	−7.588	−0.596	+0.177	7.614	−0.637	1.867	−0.353	2.004	5.610	4.588
Far-UV Band										
Z	−1.015	+0.202	−1.206	1.589	N.A.[h]	N.A.	N.A.	N.A.	N.A.	1.210
B	−0.971	+0.737	−0.468	1.306	N.A.	N.A.	N.A.	N.A.	N.A.	0.993

[a]M means monomer, Z stands for zeaxanthin, and B stands for β-cryptoxanthin. [b]Cartesian coordinates of excited-state dipole moments. [c]Magnitude of the ETDMs in the excited state. [d]Cartesian coordinates of the ground-state dipole moments. [e]Magnitude of the ground-state dipole moments. [f]Difference between the magnitudes of the excited- and ground-state dipole moments. [g]Length of the ETDMs. [h]No available.

where Φ_D is the unknown fluorescence quantum yield of the fluorophore, η is the refractive index of the environment, A is the integrated absorbance of the fluorophore, I is the integrated fluorescence intensity of the fluorophore, and the subindex "ref" indicates the same variable labels, but for the reference fluorophore.[31]

As exhibited in Table S26, the calculated Φ of BCRY in methanol was 4.343×10^{-4}. The fluorescence of carotenoids resulting from the transition between the S_2 excited state (whose electronic state is $1^1B_u^+$) and the S_1 ground state (whose electronic state is $2^1A_g^-$) is very weak, and Φ is typically 10^{-5}−10^{-4}.[88] Albeit the fluorescence quantum yield of synthetic dyes used in FRET experiments fluctuates usually within 0.12−0.80, the low quantum yield of carotenoids still enables them to participate in the harvesting and transferring of solar energy to chlorophylls with efficiencies near unity during natural photosynthesis.[89] Table S27 indicates that the computed Φ of BCRY inside the ZLCH was 1.747×10^{-4}, while Table 6 shows that the computed Φ of ZEA inside the ZLCH was 1.662×10^{-4}, decreasing in both cases by about 60% with respect to that of their counterpart in methanol.

Even though carotenoids are floppy molecules, monomers in the present study remained nearly coplanar in methanol despite being less rigid than other highly fluorescent pigments such as polycyclic aromatic hydrocarbons. The confinement of monomers in a ZLCH may protect monomers from severe rotations or vibrations of the side groups of the fluorophore, but the huge electric fields prevailing inside a ZLCH are also able to distort the molecular geometry, including the PCH, inducing nonradiated deactivation mechanisms. Many other nonradiated processes compete efficiently with the emission of light and thus reduce the fluorescence quantum yield, depending, in a complicated fashion, on the molecular structure of the monomer.[90]

κ^2 is the relative orientation factor used to estimate the alignment of ETDMs of monomers along their x molecular axes, and it ranges from 0 to 4. Averaging the donor and acceptor orientations of freely rotating monomers leads to a mean value of $\kappa^2 = 2/3$ for monomers in an isotropic medium. On the other hand, the rate of FRET from a donor D to an acceptor A in an anisotropic medium also depends on the orientation of donor and acceptor dipoles, being independent of the polarity of the medium. To calculate κ^2 for a dimer in an anisotropic matrix such as that offered by a ZLCH, it is necessary to use the following equation

$$\kappa = \cos \phi_{AD} - 3(\cos \phi_A)(\cos \phi_D) \quad (7)$$

where ϕ_{AD} is the angle between dipoles. ϕ_A is the angle between the ETDM of the acceptor A and a straight line connecting A to D, and ϕ_D is the angle between the ETDM of the donor D and a straight line connecting D to A. Two dipoles fully lined up show the following values: $\phi_{AD} = 180°$, $\phi_A = 180°$, and $\phi_D = 0°$; substituting these values into eq 7 results in the highest feasible value of 4 for κ^2.[91]

Table 7 shows that ETDMs for monomers were larger than 7.2 D, while the differences between excited- and ground-state dipole moments ($|\mu_{es} - \mu_{gs}|$) of ZEA and BCRY were 3.781 and 5.610 D, respectively. The former and latter values agree with those reported by other quantum mechanical computations, where such a difference was within 0.37−4.38 D for *N*,*N*-dimethylamino nitrile pyrene and its higher analogues in vacuum and different solvents.[92] Experimental research has also shown $\mu_{es} - \mu_{gs}$ values fluctuating within 5.39−6.32 D for a novel pyrazoline derivative in different solvents.[31] Cartesian coordinate signs of excited- and ground-state dipole moments are opposite for ZEA. A recent gas-phase theoretical study of the carotenoid peridinin demonstrated that the final value for the ETDM obeyed the following relationship: $|\mu_{es} - \mu_{gs}|/\cos \varphi$, where φ is the angle formed by both dipoles. The angle formed by the μ_{gs} of ZEA and the c-axis of the ZLCH is 70.7°, while the same angle for the μ_{es} is 4.5° (Table 7). Applying the aforementioned relationship, the magnitude of the ETDM of ZEA may still increase up to 14.801 D. In the last reference study, the theoretical relationship agreed well with Stark spectroscopic experiments.[93]

The validity of the dipole−dipole coupling theory depends on the condition that the distance between the ETDM of the two involved chromophores is large enough with respect to the length of the ETDM (l_{μ^*}).[77]

https://doi.org/10.1021/acsomega.3c01010
ACS Omega 2023, 8, 15594−15610

$$l_{\mu^*} = 3.036 \times 10^{-6}\ \text{cm}^{0.5} \times \sqrt{\frac{f}{\overline{\upsilon}}} \quad (8)$$

where l_{μ^*} is the length of the ETDM, f is the oscillator strength of the involved excited state, and $\overline{\upsilon}$ is the wavenumber of the involved excited state in cm^{-1}.

As displayed in Table 7, ETDM lengths for ZEA and BCRY are 4.417 and 4.588 Å, respectively. The shortest possible core-to-core distance between the monomers inside the ZLCH is 30.178 Å, and the l_{μ^*} values represent 14.6 and 15.2% of the latter core-to-core distance. Perylene bisimide, a well-established synthetic dye in FRET experiments, has a l_{μ^*} of 1.9 Å, corresponding to 8.6% of that of its shortest possible core-to-core distance of 22 Å.[14] It means that the distance between the monomers of interest in the ZLCH was in general large enough so that the dipole−dipole coupling approach was a good approximation. The average magnitude and length of ETDMs in B2 corresponded to 19.4 and 1.2% of those exhibited in B1, respectively.

Table 8 contains the angles formed between the ETDMs and the c-axis of the ZLCH; these values were 4.5 and 2.5° for ZEA and BCRY in B1, respectively. Pyronine and oxonine, two synthetic pigments studied in depth in energy-transfer experiments, showed ϕD and ϕA values of 30 and 40°,[94] derived from space-filling arguments, respectively. As the lower the value of these angles, the better the alignment of EDTMs, it was expected to obtain a value for the ETDM relative orientation factor very close to the ideal value of 4 (κ^2 = 3.954). Regarding ϕD and ϕA values for ETDMs in B2, they were 11.3 and 37.2° for ZEA and BCRY, respectively. Albeit the last values were much higher than those of their counterparts in B1, they still match with those of the pyronine−oxonine dimer, and ETDMs of monomers in B2 were yet capable of reaching a κ^2 of 2.086. Table S28 shows the same information as that shown in Table 8, but for the dimer BCRY/ZEA.

Table 8. Relative Orientation Factors of the Electronic Transition Dipole Moments of Dyes in the Zeolite-LTL Nanochannel

donor ES[a]	acceptor ES[b]	ϕ_D[c] [deg]	ϕ_A[d] [deg]	ϕ_{DA}[e] [deg]	κ^2[f]
Main Spectral Band					
1	1	4.5	2.5	2.0	3.954
Far-UV Band					
4	4	11.3	37.2	26.0	2.086

[a]$S_0 \rightarrow S_2$ excited state of zeaxanthin. [b]$S_0 \rightarrow S_2$ excited state of β-cryptoxanthin. [c]Angle formed between the ETDM of the donor and the c-axis of the zeolite-LTL nanochannel. [d]Angle formed between the ETDM of the acceptor and the c-axis of the zeolite-LTL nanochannel. [e]Angle formed between the ETDMs of the donor and the acceptor. [f]Relative orientation factor between the ETDMs of the donor and the acceptor.

Eventually, Figure 4 depicts the location of dipole moments within both monomers, drawing angles and lengths to the scale of the full composite. Ground-state dipole moments were near the molecular center between the C15−C15′ bond. ETDMs involved in the main electronic transition $S_2 \leftarrow S_0$ were conveniently close to each other, a desirable feature to increase the FRET efficiency. ETDMs responsible for the electronic transition that gave rise to B2 were in between the ground state and the main ETDMs. Red and green arrows had the opposite direction in ZEA.

As shown in Table S29 and 9, Ro for the dimer in methanol was 18.656 Å, while it was 24.937 Å for the dimer in the ZLCH. A highly anisotropic medium such as the ZLCH yielded a better Förster radium owing to two main reasons; first, κ^2 in the ZLCH is almost six times higher than that of its counterpart in methanol, and second, the molar absorptivity of monomers inside the ZLCH is threefold higher than that of monomers in methanol. The last consideration enabled the increase of the spectral overlap from $1.382 \times 10^{15}\ \text{M}^{-1}\ \text{cm}^{-1}\ \text{nm}^4$ in the uncorrected absorption spectrum to the final value of $4.146 \times 10^{15}\ \text{M}^{-1}\ \text{cm}^{-1}\ \text{nm}^4$ in the corrected one. Ro of B2 is slightly higher than that of the half of B1. Experimental Ro values for two synthetic-dye dimers in a (K^+)-zeolite-LTL were 17.9 and 22.0 Å, agreeing well with the one found herein.[25,26] Table S30 displays the same information as that shown in Table 9, but for the dimer BCRY/ZEA.

The following equation allows the calculation of the probability that FRET occurs

$$P = \frac{1}{1 + (R/Ro)^{\alpha}} \quad (9)$$

where P is the probability that FRET occurs, R is the distance between the ETDMs, Ro is the Förster radium, and α represents the dimensional system in which the molecules are embedded. In the case of a one-dimensional system like the ZLCH, α is equal to two, whereas in the case of an isotropic system like methanol, it is equal to six.[58]

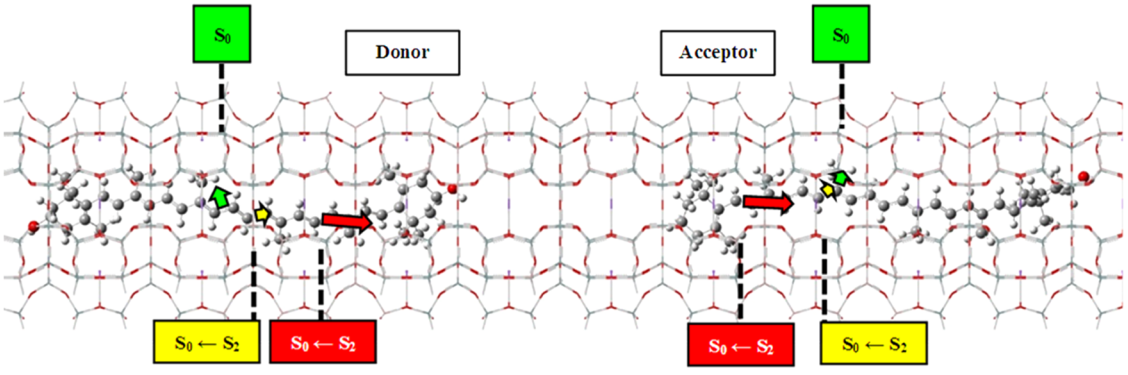

Figure 4. Zeaxanthin (left) and β-cryptoxanthin (right) inside the zeolite-LTL nanochannel. Dipole moments in the ground state, B1 excited state, and B2 excited state appear in green, yellow, and red, respectively. The origins of dipole moments for Zeaxanthin/β-cryptoxanthin in the ground state, B1 excited state, and B2 excited state are located at C14′−C15′/C14′−C20, C10′−C11′/C7−C8, and C14−C15/C12′−C13′, respectively.

https://doi.org/10.1021/acsomega.3c01010
ACS Omega 2023, 8, 15594−15610

Table 9. Förster Radius of Monomers in the Individual Composites

dimer[a]	J (M^{-1} cm^{-1} nm^4)[b]	Φ_D[c]	κ^2[d]	η[e]	Ro (Å)[f]
		Total Spectrum			
Z·B	4.146×10^{15}	1.662×10^{-4}	3.956	1	24.937
		Far-UV band			
Z·B	1.790×10^{14}	1.662×10^{-4}	2.113	1	13.305

[a]Donor and acceptor pair at the left and right sides of the point, respectively, where B stands for β-cryptoxanthin and Z stands for zeaxanthin. [b]Spectral overlap of the normalized emission spectrum of the donor and the corrected absorption spectrum of the acceptor. [c]Fluorescence quantum yield of the donor. [d]Relative orientation factor of ETDMs of monomers in the dimer. [e]Refractive index of the environment that surrounds the monomers. [f]Förster radius of the dimer.

Table S31 shows that the FRET efficiency ($E_{FRET} = P \times 100$) of the dimer BCRY/ZEA in methanol (D17) was 8.7%, while B2 contributed almost 46% to the latter FRET efficiency. Table 10 displays the final FRET efficiency of the dimer ZEA/BCRY in the ZLCH (C17, because this composite obtained the lowest interaction energy), which is 40.9%. Noticeably, B2 contributed with almost 20% to this final FRET efficiency, highlighting the great importance of this far-UV band, not only to identify carotenoids but also improving the energy-transfer mechanism. Table S32 shows the same information as that of Table 10, but for the dimer BCRY/ZEA.

Table 10. FRET Efficiency of the Dimer Zeaxanthin/β-Cryptoxanthin in the Zeolite-LTL Nanochannel

composite	R [Å][a]	Ro [Å][b]	E_{FRET} [%][c]
	Complete Spectra		
C10	27.204	24.937	45.7
C14	28.546	24.937	43.3
C17	29.999	24.937	40.9
C21	36.545	24.937	31.8
	Far-UV Band		
C10	42.171	13.305	9.1
C14	43.513	13.305	8.5
C17	44.966	13.305	8.0
C21	51.512	13.305	6.3

[a]Distance between ETDMs of both monomers. [b]Förster radius of dimers. [c]FRET efficiency of dimers.

Confinement of monomers excerpted by the ZLCH was decisive to obtain a respectable FRET efficiency of 40.9%. Although the fluorescence quantum yield of the donor inside the ZLCH was too low (1.662×10^{-4}), this value came from the use of an experimental reference compound in solution because there are no experimental data of carotenoids inside a ZLCH. Therefore, the value needs a validation by means of an experiment, given that 1,1′-diethyl-2,2′-cyanine iodide, which is not fluorescent experimentally in chloroform, exhibited fluorescence inside a K^+-ZL.[25]

ZLCH confinement also allowed a large hypsochromic shift in monomers' spectra, increasing their ability to harvest higher-energy photons. In addition, the ZLCH prevented monomers' side groups from undergoing severe rotations and vibrations, enabling monomers' ETDMs to reach a relative orientation factor very close to the ideal value of four ($\kappa^2 = 3.956$). Proximity of monomers' hydrogen atoms to the framework's oxygen atoms may form hydrogen bonds, while interactions between extraframework cations and the oxygen atoms of monomers (δ^-) may establish ion−dipole interactions. Huge electric fields prevailing inside the ZLCH conferred optical properties to our monomers very different from that observed in solution. One of the most important effects of the ZLCH confinement deals with its protection against undesirable reactions such as degradation, oxidation, and isomerization; this key protection would allow monomers to harvest sunlight and transfer the FRET energy, without getting affected by these chemical changes.

Highly fluorescent synthetic donors have already achieved FRET efficiencies near unity ($E_{FRET} \approx 100\%$). Nevertheless, some natural dyes such as the xanthophylls assessed here, which participate in natural photosynthesis, may yet participate in a zeolite-LTL-based antenna complex. This complex would harvest sunlight strongly in the ranges of 384−477 and 245−290 nm, despite hosting guests with very small fluorescence quantum yields (10^{-5}−10^{-4}). A hypothetical natural donor with the highest possible Φ of 1 would have obtained values of ≈93% and 106 Å for E_{FRET} and Ro, respectively, employing the remaining parameters of this study. However, as non-fluorescent natural dyes are among the most abundant and ubiquitous natural pigments, they should be considered by researchers. It is very important to search for other natural dyes beyond photosynthetic pigments with higher Φ that fit into zeolite-LTL nanochannels and inside other advanced anisotropic host systems. Finally, the employment of natural dyes guarantees that any eventual antenna complex will be more economic and environment-friendly.

The major limitations of this work came from restraints in computational resources, e.g., modeling the whole dimer in methanol would have been the best choice rather than simulating monomers in methanol separately because this approach neglected the contribution of the interaction energy. Although the 3-21* basis set could describe accurately ground-state geometries of dimers, a higher degree of accuracy could be reached with the use of a bigger basis set such as 6-31G. Simulation of dimers and monomers in the zeolite-LTL nanochannel without fixing all nanochannel's atoms in their crystallographic positions would allow one to study interactions between monomers and the nanochannel's inner walls. Computing excitation energies with individual composites instead of complete composites again neglected the contribution of interaction energies to the final spectra. The use of solvents instead of modeling dimers and monomers only in the gas phase is necessary. Anyway, we attempted to address all of the drawbacks discussed in this paragraph, but it was impossible for us because no sample converged with the available computational resources.

The ratio R/Ro for C17 (1.2) was somewhat high with respect to that of synthetic dyes. Assuming average values for R and Ro of 15 and 45 Å, respectively, R/Ro would be 0.3, and the lower this ratio, the higher the FRET efficiency. Thus, shorter natural dyes with higher fluorescence quantum yields should remain a priority for those investigating natural dye antenna systems.

Ultimately, our group employed only two molecules inside the host system, but the intensity of the energy delivered by a zeolite-LTL-based antenna increases as the ratio of the donor/acceptor increases. Other phenomena of photophysical interest such as self-absorption, re-emission, speed of energy migration, and the possible formation of J-aggregates require the use of more than two molecules. The size of a zeolite-LTL

https://doi.org/10.1021/acsomega.3c01010
ACS Omega 2023, 8, 15594−15610

nanochannel would also need to be higher than that utilized in this study in order to host more than two molecules (>150 Å). To reach the improvements suggested in this work, others should have higher computational resources, but even then, simulating molecules as large as those employed here may still be an unfeasible task for the current state-of-art modeling. As the overall study was strictly theoretical, suitable experiments must reveal how quantitative and qualitative its nature was.

CONCLUSIONS

A composite containing all-*trans*-zeaxanthin as a donor, all-*trans*-β-cryptoxanthin as an acceptor, and a zeolite-LTL nanochannel as a host system showed theoretically its capacity to harvest and transfer energy with an efficiency of 40.9%. As the same efficiency for the dimer in methanol was 8.0%, the work established quantitatively how a host system with such optical anisotropy and one-dimensionality could increase the FRET efficiency of even nonfluorescent and long natural guests. The Förster radius, the spectral overlap, the ETDM's relative orientation factor, and the distance between ETDMs of the dimer were 24.937 Å, 4.146 × 10^{15} M^{-1} cm^{-1} nm^4, 3.954, and 29.999 Å, respectively. *R*/*Ro* was somewhat high (1.2), and the search for shorter natural dyes with higher fluorescence quantum yields should be the target. The competitive spectral overlap came from the fact that the molar absorptivity of a monomer in a nanochannel is threefold higher than that of the monomer in a solution. Geometrical parameters of zeaxanthin computed with the CAM-B3LYP/3-21G* level of theory agreed with those reported for its crystalline structure. CL and iM deformations of monomers did not match with distortion energies, evidencing the need for future QSAR analysis. The host system induced unusual changes in monomers' optical properties, a *cis*-like region appeared despite the all-*trans* nature of the original dyes, there were large hypsochromic shifts of λ_{max} in emission spectra (−40 nm) and absorption spectra (−60 to −70 nm), and the far-UV band of pigments remained in the same position in both methanol and the ZLCH. Contribution of the latter band to the FRET efficiency was 19.5%. The composite is capable of emitting and harvesting sunlight strongly at bandwidths of 466−588 and 393−477 nm, respectively. We strongly believe that the proposed methodology employed herein paved the way for others to assess computationally geometrical and optical properties of carotenoids, carotenoid-like molecules, and polyenes inside a zeolite-LTL nanochannel. This investigation calculated a respectable FRET efficiency of 40.9% for a dimer built with nonfluorescent natural photosynthetic dyes for the first time. C17 may participate in an eventual antenna complex, where the composite contributed to improving the antenna's cost and environment-friendliness. Research of suitable natural dyes inside composites based on zeolite-LTL should remain a very dynamic field.

ASSOCIATED CONTENT

Supporting Information

The Supporting Information is available free of charge at https://pubs.acs.org/doi/10.1021/acsomega.3c01010.

Geometrical parameters of monomers and dimers such as dihedral angles, coplanarity loss, end-to-end distances, and atom-to-atom distances.; and optical parameters of monomers and dimers such as fluorescence quantum yields, relative orientation factors, spectral overlaps, Förster radii, and FRET efficiencies (PDF)

AUTHOR INFORMATION

Corresponding Author

Jesús Francisco Monzón-Bensojo − *Universidad Juárez del Estado de Durango (UJED), Facultad de Ciencias Químicas, C.P. 34120 Victoria de Durango, Durango, México;* orcid.org/0000-0001-8658-653X; Email: mcjfmb@outlook.com

Authors

Manuel Alberto Flores-Hidalgo − *Universidad Juárez del Estado de Durango (UJED), Facultad de Ciencias Químicas, C.P. 34120 Victoria de Durango, Durango, México*

Ruth Flores-Barraza − *Universidad Juárez del Estado de Durango (UJED), Facultad de Ciencias Químicas, C.P. 34120 Victoria de Durango, Durango, México*

Diana Barraza-Jiménez − *Universidad Juárez del Estado de Durango (UJED), Facultad de Ciencias Químicas, C.P. 34120 Victoria de Durango, Durango, México*

Complete contact information is available at: https://pubs.acs.org/10.1021/acsomega.3c01010

Author Contributions

The manuscript was written through contributions of all authors. All authors have given approval to the final version of the manuscript. All authors contributed equally.

Funding

J.F.M.-B., M.A.F.-H., R.F.-B., and D.B.-J. received funding from CONACYT (Mexican Science and Technology National Council) by means of an authorized SEP-CB (Basic Science-Public Education Ministry) project grant 158307, with which this research work was completed.

Notes

The authors declare no competing financial interest.

ACKNOWLEDGMENTS

J.F.M.-B., M.A.F.-H., R.F.-B., and D.B.-J. thank CONACYT (Mexican Science and Technology National Council) for authorizing the project grant 158307. They also acknowledge the Scientific Computational Laboratory at FCQ-UJED for computational resources and the Academic Group UJED-CA-129 for valuable discussions. Jesús Francisco Monzón-Bensojo appreciates the Doctorate Scholarship received on behalf of CONACYT.

ABBREVIATIONS

BCRY, all-*trans*-β-cryptoxanthin; ZEA, all-*trans*-zeaxanthin; LTL, Linde type L; ZLCH, zeolite-LTL nanochannel; IM, intermolecular; iM, intramolecular; IC, individual composite; DX, dimer with an end-to-end intermolecular distance equal to *X* Å; CL, coplanarity loss; PCH, polyene chain; B1, main band of spectra; B2, far-UV band of spectra; B3, *cis*-like region of spectra

REFERENCES

(1) Dincer, I.; Colpan, C.; Kadioglu, F. *Causes, Impacts and Solutions to Global Warming*, 1st ed.; Springer-Verlag: New York, 2013; pp 3−362.

(2) Jacobson, M. *Air Pollution and Global Warming History, Science, and Solutions*, 2nd ed.; Cambridge University Press: Cambridge, 2012; pp 309−311.
(3) Benda, V.; Černá, L. PV cells and modules − State of the art, limits and trends. *Heliyon* **2020**, *6*, No. e05666.
(4) Meyer Burger Official Website, accessed on March the 11th, 2023; https://www.meyerburger.com/.
(5) Förster, T. Zwischenmolekulare Energiewanderung und Fluoreszenz. *Ann. Phys.* **1948**, *437*, 55−75.
(6) Rozhkova, E.; Ariga, K. *From Molecules to Materials: Pathways to Artificial Photosynthesis*, 1st ed.; Springer International Publishing: Dordrecht, 2015; pp 1−98.
(7) Calzaferri, G. Artificial photosynthesis. *Top. Catal.* **2010**, *53*, 130−140.
(8) Calzaferri, G. Guests in Nanochannels of Zeolite L. In *Dyes and Photoactive Molecules in Microporous Systems. Structure and Bonding. Structure 183*, 1st ed.; Martínez-Martínez, V.; López, F., Eds.; Springer: Cham, 2020; pp 1−73.
(9) Hashimoto, S. Zeolite photochemistry: Impact of zeolites on photochemistry and feedback from photochemistry to zeolite Science. *J. Photochem. Photobiol., C* **2003**, *4*, 19−49.
(10) Zabala Ruiz, A.; Li, H.; Calzaferri, G. Organizing supramolecular functional dye-zeolite crystals. *Angew. Chem., Int. Ed.* **2006**, *45*, 5282−5287.
(11) Gfeller, N.; Megelski, S.; Calzaferri, G. Fast Energy Migration in Pyronine-Loaded Zeolite L Microcrystals. *J. Phys. Chem. B* **1999**, *103*, 1250−1257.
(12) Pauchard, M.; Devaux, A.; Calzaferri, G. Dye-Loaded Zeolite L Sandwiches as Artificial Antenna Systems for Light Transport. *Chem. - Eur. J.* **2000**, *6*, 3456−3470.
(13) Davydov, A. S. The theory of molecular excitons. *Soviet Phys.-Usp.* **1964**, *7*, 145−178.
(14) Busby, M.; Devaux, A.; Blum, C.; Subramaniam, V.; Calzaferri, G.; De Cola, L. Interactions of Perylene Bisimide in the One-Dimensional Channels of Zeolite L. *J. Phys. Chem. C* **2011**, *115*, 5974−5988.
(15) Calzaferri, G.; De Cola, L.; Busby, M.; Blum, C.; Subramaniam, V. Method for Intercalating Chromophores into Zeolite-L. U.S. Patent US8,173,041 B2, 2012.
(16) Busby, M.; Blum, C.; Tibben, M.; Fibikar, S.; Calzaferri, G.; Subramaniam, V.; De Cola, L. Time, Space, and Spectrally Resolved Studies on J-Aggregate Interactions in Zeolite L Nanochannels. *J. Am. Chem. Soc.* **2008**, *130*, 10970−10976.
(17) Calzaferri, G.; Kunzmann, A.; Brühwiler, D. Local j-Coupling Dye-Zeolite Antenna Composite Materials. U.S. Patent US009724433B2, 2017.
(18) Gigli, L.; Arletti, R.; Fois, E.; Tabacchi, G.; Quartieri, S.; Dmitriev, V.; Vezzalini, G. Unravelling the High-Pressure Behaviour of Dye-Zeolite L Hybrid Materials. *Crystals* **2018**, *8*, No. 79.
(19) Gigli, L.; Arletti, R.; Tabacchi, G.; Fabbiani, M.; Vitillo, J.; Martra, G.; Devaux, A.; Miletto, I.; Quartieri, S.; Calzaferri, G.; Fois, E. Structure and Host-Guest Interactions of Perylene- Diimide Dyes in Zeolite L Nanochannels. *J. Phys. Chem. C.* **2018**, *122*, 3401−3418.
(20) Tabacchi, G.; Calzaferri, G.; Fois, E. One-Dimensional Self-Assembly of Perylene-Diimide Dyes by Unidirectional Transit of Zeolite Channel Openings. *Chem. Commun.* **2016**, *52*, 11195−11198.
(21) Tabacchi, G.; Fois, E.; Calzaferri, G. Structure of Nanochannel Entrances in Stopcock-Functionalized Zeolite L Composites. *Angew. Chem., Int. Ed.* **2015**, *54*, 11112−11116.
(22) Gigli, L.; Arletti, R.; Tabacchi, G.; Fois, E.; Vitillo, J.; Martra, G.; Agostini, G.; Quartieri, S.; Vezzalini, G. Close-Packed Dye Molecules in Zeolite Channels Self-Assemble into Supramolecular Nanoladders. *J. Phys. Chem. C* **2014**, *118*, 15732−15743.
(23) Fois, E.; Tabacchi, G.; Devaux, A.; Belser, P.; Brühwiler, D.; Calzaferri, G. Host-guest interactions and orientation of dyes in the one-dimensional channels of zeolite L. *Langmuir* **2013**, *29*, 9188−9198.
(24) Fois, E.; Tabacchi, G.; Calzaferri, G. Orientation and Order of Xanthene Dyes in the One-Dimensional Channels of Zeolite L: Bridging the Gap between Experimental Data and Molecular Behavior. *J. Phys. Chem. C* **2012**, *116*, 16784−16799.
(25) Insuwan, W.; Rangsriwatananon, K.; Meeprasert, J.; Namuangruk, S.; Surakhot, Y.; Kungwan, N.; Jungsuttiwong, S. Combined experimental and theoretical investigation on Fluorescence Resonance Energy Transfer of dye loaded on LTL zeolite. *Microporous Mesoporous Mater.* **2017**, *241*, 372−382.
(26) Insuwan, W.; Jungsuttiwong, S.; Rangsriwatananon, K. Host−guest composite materials of dyes loaded zeolite LTL for antenna applications. *J. Lumin.* **2015**, *161*, 31−36.
(27) Insuwan, W.; Rangsriwatananon, K.; Meeprasert, J.; Namuangruk, S.; Surakhot, Y.; Kungwan, N.; Jungsuttiwong, S. Combined experimental and theoretical investigation on Photophysical properties of trans-azobenzene confined in LTL zeolite: Effect of cis-isomer forming. *Microporous Mesoporous Mater.* **2014**, *197*, 348−357.
(28) Chung, L. W.; Sameera, W.; Ramozzi, R.; Page, A.; Hatanaka, M.; Petrova, G.; Harris, T.; Li, X.; Ke, Z.; Liu, F.; Li, H-B.; Ding, L.; Morokuma, K. The ONIOM Method and Its Applications. *Chem. Rev.* **2015**, *115*, 5678−5796.
(29) Green, M.; Dunlop, E.; Hohl-Ebinger, J.; Yoshita, M.; Kopidakis, N.; Hao, X. Solar cell efficiency tables (version 57). *Prog. Photovoltaics* **2021**, *29*, 3−15.
(30) Rhodes, C. J. Endangered elements, critical raw materials and conflict minerals. *Sci. Prog.* **2019**, *102*, 304−350.
(31) Khan, S.; Ullah, Q.; Syed, S.; Alimuddin; Abdulraheem, S. A.; Almalki, A.; Obaid, R.; Alsharif, M.; Alfaifi, S.; Kumar, S. Aggregated Synthesis, Physicochemical investigation and optical properties of pyrazoline derivative: A Donor-π-Acceptor chromophore. *J. Mol. Struct.* **2021**, *1227*, No. 129667.
(32) Richhariya, G.; Kumar, A.; Tekasakul, P.; Gupta, B. Natural dyes for dye sensitized solar cell: A review. *Renewable Sustainable Energy Rev.* **2017**, *69*, 705−718.
(33) Britton, G.; Liaaen-Jensen, S.; Pfander, H. *Carotenoids Spectroscopy*, 1st ed.; Birkhäuser: Verlag: Basel, 1995; Vol. *1B*, pp 1−360.
(34) Britton, G.; Liaaen-Jensen, S.; Pfander, H. *Carotenoids Handbook*, 1st ed.; Birkhäuser: Verlag: Basel, 2004; pp 51−212.
(35) Polívka, T.; Sundström, V. Ultrafast dynamics of carotenoid excited states-from solution to natural and artificial systems. *Chem. Rev.* **2004**, *104*, 2021−2071.
(36) Frisch, M.; Trucks, G.; Schlegel, H.; Scuseria, G.; Robb, M.; Cheeseman, J.; Scalmani, G.; Barone, V.; Petersson, G.; Nakatsuji, H. et al. *Gaussian 16*, revision C.01, Gaussian Inc.: Wallingford, CT, 06492 USA, 2016.
(37) Boys, S.; Bernardi, F. The calculation of small molecular interactions by the differences of separate total energies. Some procedures with reduced errors. *Mol. Phys.* **1970**, *19*, 553−566.
(38) Preus, S. ale − UV-Vis-IR Spectral Software 1.2, Fluor Tools, Available online: www.fluortools.com (accessed on October the 29th, 2022).
(39) Monzón, J.; Flores, M.; Barraza, D. Photosynthetic Pigments with Potential for a Photosynthetic Antenna: A DFT Analysis. *Int. J. Photoenergy* **2019**, No. 7432848.
(40) Thompson, M. *Molecular Docking Using Argus Lab, an Efficient Shape-Based Search Algorithm and the AScore Scoring Function*; ACS Meeting: Philadelphia, 172, CINF 42, PA, 2004.
(41) Yanai, T.; Tew, D.; Handy, N. A new hybrid exchange-correlation functional using the Coulomb attenuating method (CAM-B3LYP). *Chem. Phys. Lett.* **2004**, *393*, 51−57.
(42) McLean, A. D.; Chandler, G. Contracted Gaussian basis sets for molecular calculations. I. Second row atoms, Z = 11−18. *J. Chem. Phys.* **1980**, *72*, 5639−5648.
(43) Jacquemin, D.; Perpète, E.; Scuseria, G.; Ciofini, I.; Adamo, C. TD-DFT performance for the visible absorption spectra of organic dyes: Conventional versus long-range hybrids. *J. Chem. Theory Comput.* **2008**, *4*, 123−135.
(44) Bartalucci, G.; Coppin, J.; Fisher, S.; Hall, G.; Helliwell, J.; Helliwell, M.; Liaaen-Jensen, S. Unravelling the chemical basis of the

https://doi.org/10.1021/acsomega.3c01010
ACS Omega 2023, 8, 15594−15610

bathochromic shift in the lobster carapace; new crystal structures of unbound astaxanthin, canthaxanthin and zeaxanthin. *Acta Crystallogr., Sect. B: Struct. Sci.* **2007**, *63*, 328−337.
(45) Bálint, D.; Jäntschi, L. Comparison of molecular geometry optimization methods based on molecular descriptors. *Mathematics* **2021**, *9*, 2855.
(46) Baniya, D. The Hydrogen Passivated Graphene Cluster and its Stability - First Principle DFT (B3LYP) Levels of Approximation with the Basis Set 3-21G. *Kathford J. Eng. Manage.* **2018**, *1*, 5−10.
(47) Chrząstek, L.; Peszke, J.; Śliwa, W. DFT B3-LYP/3-21G geometry optimisation and effective charge values calculations for azodiazaphenanthrenes and acylaminodiazaphenanthrenes. *J. Mol. Struct.* **2007**, *830*, 94−99.
(48) Zandler, M. E.; D'Souza, F. The remarkable ability of B3LYP/3-21G(*) calculations to describe geometry, spectral and electrochemical properties of molecular and supramolecular porphyrin-fullerene conjugates. *C. R. Chim.* **2006**, *9*, 960−981.
(49) Zheng, G.; Irle, S.; Morokuma, K. Performance of the DFTB method in comparison to DFT and semiempirical methods for geometries and energies of C20-C86 fullerene isomers. *Chem. Phys. Lett.* **2005**, *412*, 210−216.
(50) Fabian, J. Electronic excitation of sulphur-organic compounds - Performance of time-dependent density functional theory. *Theor. Chem. Acc..* **2001**, *106*, 199−217.
(51) Curtiss, L. A.; McGrath, M.; Blaudeau, J-P.; Davis, N.; Binning, R.; Radom, L. Extension of Gaussian-2 theory to molecules containing third-row atoms Ga-Kr. *J. Chem. Phys.* **1995**, *103*, 6104−6113.
(52) Casida, M. *Time-Dependent Density Functional Response Theory for Molecules. In Recent Advances in Density Functional Theory*, 1st ed.; Chong, D., Ed.; World Scientific Publishing Co Pte Ltd.: 5 Toh Tuck Link, 1995; pp 155−192.
(53) Grimme, S. A simplified Tamm-Dancoff density functional theory approach for the electronic excitation spectra of very large molecules. *J. Chem. Phys.* **2013**, *138*, No. 244104.
(54) Mennucci, B. Polarizable continuum model. *Wiley Interdiscip. Rev.: Comput. Mol. Sci.* **2012**, *2*, 386−404.
(55) Baerlocher, C.; McCusker, L. Database of Zeolite Structures. Structure Commission of the International Zeolite Association (IZA-SC), 2017, Available online: http://www.iza-structure.org/databases/ (accessed on October 29, 2022).
(56) Allinger, N. Calculation of Molecular Structure and Energy by Force-Field Methods. In *Advances in Physical Organic Chemistry*, 1st ed.; Gold, V.; Bethell, D., Eds.; Academic Press Inc.: London, 1976; Vol. *13*, pp 2−26 31.
(57) Rappe, A. K.; Casewit, C.; Colwell, K.; Goddard, W.; Skiff, W. UFF, a Full Periodic Table Force Field for Molecular Mechanics and Molecular Dynamics Simulations. *J. Am. Chem. Soc.* **1992**, *114*, 10024−10035.
(58) Hanwell, M.; Curtis, D.; Lonie, D.; Vandermeersch, T.; Zurek, E.; Hutchison, G. Avogadro: An open-source molecular builder and visualization tool v.1.2.0. An advanced semantic chemical editor, visualization and analysis platform. *J. Cheminf.* **2012**, *4*, No. 17.
(59) Sotoyama, W.; Sato, H.; Matsuura, A.; Sawatari, N. Ab initio configuration interaction singles (CIS) study on polycyclic aromatic molecules (II): Predicting fluorescence quantum yields by calculating the excitation energies. *J. Mol. Struct.: THEOCHEM* **2005**, *756*, 35−38.
(60) Tirapattur, S.; Belletête, M.; Leclerc, M.; Durocher, G. Study of excited state properties of oligofluorenes by the singles configuration interaction (CIS) theoretical approach. *J. Mol. Struct.: THEOCHEM* **2003**, *625*, 141−148.
(61) Foresman, J. B.; Head-Gordon, M.; Pople, J.; Frisch, M. Toward a systematic molecular orbital theory for excited states. *J. Phys. Chem. A* **1992**, *96*, 135−149.
(62) Jaskolski, M.; Gilski, M.; Dauter, Z.; Wlodawer, A. Stereochemical restraints revisited: How accurate are refinement targets and how much should protein structures be allowed to deviate from them? *Acta Crystallogr., Sect. D: Biol. Crystallogr.* **2007**, *63*, 611−620.
(63) Brzezinski, K.; Brzuszkiewicz, A.; Dauter, M.; Kubicki, M.; Jaskolski, M.; Dauter, Z. High regularity of Z-DNA revealed by ultra-high-resolution crystal structure at 0.55 Å. *Nucleic Acids Res.* **2011**, *39*, 6238−6248.
(64) Cousins, K. R. Computer review of ChemDraw ultra 12.0. *J. Am. Chem. Soc.* **2011**, *133*, 8388.
(65) Lakowicz, J. *Principles of Fluorescence Spectroscopy*, 3rd ed.; Springer Science+Business Media, LLC: New York, 2006; pp 443−468.
(66) Ramamurthy, V.; Inoue, Y. *Supramolecular Photochemistry: Controlling Photochemical Processes*, 1st ed.; John Wiley & Sons, Inc.: New Jersey, 2011; pp 285−388.
(67) Intermolecular Interactions. In *Handbook of Computational Chemistry*, 1st ed.; Misquitta, A.; Leszczynski, J., Eds.; Springer Science+Business Media Dordrecht: Cham, 2017; pp 295−335.
(68) Alvarado, M.; Gallo, M.; Lopez, P.; Flores, N.; Glossman, D. Study of the interaction between the conjugated fluorescein and dabcyl system, using fluorescene quenching method. *J. Mol. Model.* **2012**, *18*, 4113−4120.
(69) Zhang, D. W.; Xiang, Y.; Zhang, J. New advance in computational chemistry: Full quantum mechanical ab initio computation of streptavidin - Biotin interaction energy. *J. Phys. Chem. B* **2003**, *107*, 12039−12041.
(70) Bezerra, K. S.; Oliveira, J.; Lima, J.; Albuquerque, E.; Caetano, E.; Freirec, V.; Fulco, U. Quantum binding energy features of the T3-785 collagen-like triple-helical peptide. *RSC Adv.* **2017**, *7*, 2817−2828.
(71) Calzaferri, G.; K Lutkouskaya, K. Mimicking the antenna system of green plants. *Photochem. Photobiol. Sci.* **2008**, *7*, 879−910.
(72) Gruszecki, W. I.; Bogumil, Z.; Leblanc, R. Fluorescence of zeaxanthin and violaxanthin in aggregated forms. *Chem. Phys. Lett.* **1990**, *171*, 563−568.
(73) Staleva, H.; Zeeshan, M.; Chábera, P.; Partali, V.; Sliwka, H-R.; Polívka, T. Ultrafast Dynamics of Long Homologues of Carotenoid Zeaxanthin. *J. Phys. Chem. A* **2015**, *119*, 11304−11312.
(74) Zang, L.-Y.; Sommerburg, O.; van Kuijk, F. Absorbance changes of carotenoids in different solvents. *Free Radical Biol. Med.* **1997**, *23*, 1086−1089.
(75) Murillo, E. Far UV peaks contribute for identification of carotenoids E/Z isomers. *J. Food Compos. Anal.* **2018**, *67*, 159−162.
(76) Chhabra, D.; dos Remedios, C.*Fluorescence Resonance Energy Transfer, Encyclopaedia of Life Sciences*; Nature Publishing Group, 2001; pp 1−9.
(77) Calzaferri, G.; Huber, S.; Maas, H.; Minkowski, C. Host-guest antenna materials. *Angew. Chem., Int. Ed.* **2003**, *42*, 3732−3758.
(78) Maas, H.; Calzaferri, G. Trapping energy from and injecting energy into dye-zeolite Nanoantennae. *Angew. Chem., Int. Ed.* **2002**, *41*, 2284−2288.
(79) Gupta, P.; Sreelakshmi, Y.; Sharma, R. A rapid and sensitive method for determination of carotenoids in plant tissues by high performance liquid chromatography. *Plant Methods* **2015**, *11*, No. 5.
(80) Rhodes, C. J. Electric fields in zeolites: Fundamental features and environmental implications. *Chem. Pap.* **2016**, *70*, 4−21.
(81) Preuss, E.; Linden, G.; Peuckert, M. Model calculations of electrostatic fields and potentials in faujasite type zeolites. *J. Phys. Chem. B* **1985**, *89*, 2955−2961.
(82) Bussemer, B.; Munsel, D.; Wünscher, H.; Mohr, G.; Grummt, U. Electronic properties of neutral dyes in the channels of zeolite L: A combined spectroscopic and quantum chemical study. *J. Phys. Chem. B* **2007**, *111*, 8−15.
(83) Hashimoto, H.; Uragami, C.; Yukihira, N.; Gardiner, A.; Cogdell, R. Understanding/unravelling carotenoid excited singlet states. *J. R. Soc., Interface* **2018**, *15*, No. 20180026.
(84) Kurashige, Y.; Nakano, H.; Nakao, Y.; Hirao, K. The $\pi \rightarrow \pi^*$ excited states of long linear polyenes studied by the CASCI-MRMP method. *Chem. Phys. Lett.* **2004**, *400*, 425−429.
(85) Wang, P.; Nakamura, R.; Kanematsu, Y.; Koyama, Y.; Nagae, H.; Nishio, T.; Hashimoto, H.; Zhang, J-P. Low-lying singlet states of carotenoids having 8-13 conjugated double bonds as determined by

https://doi.org/10.1021/acsomega.3c01010
ACS Omega 2023, 8, 15594−15610

electronic absorption spectroscopy. *Chem. Phys. Lett.* **2005**, *410*, 108−114.
(86) Dexter, D. L. A Theory of Sensitized Luminescence in Solids. *J. Chem. Phys.* **1953**, *21*, 836−850.
(87) Nielsen, A.; Kuzmanich, G.; Garcia-Garibay, M. Quantum Chain Reaction of Tethered Diarylcyclopropenones in the Solid State and Their Distance-Dependence in Solution Reveal a Dexter S_2-S_2 Energy-Transfer Mechanism. *J. Phys. Chem. A* **2014**, *118*, 1858−1863.
(88) Landrum, J. *Carotenoids: Physical, Chemical, and Biological Functions and Properties.*, 1st ed.; CRC Press: Florida, 2009; p 89.
(89) Taiz, L.; Zeiger, E. *Plant Physiology*, 4th ed.; Sinauer Associates Inc: Sunderland, 2006; p 11.
(90) Sauer, M.; Hofkens, J.; Enderlein, J. *Handbook of Fluorescence Spectroscopy and Imaging: From Single Molecules to Ensembles*, 1st ed.; Wiley-VCH Verlag GmbH & Co. KGaA: Weinheim, 2011; p 22.
(91) Pessarakli, M. *Handbook of Photosynthesis*, 2nd ed.; Taylor & Francis: New York, 2005; p 82.
(92) Jana, D.; Jana, S. Donor-Pyrene-Acceptor Distance-Dependent Intramolecular Charge-Transfer Process: A State-Specific Solvation Preferred to the Linear-Response Approach. *ACS Omega* **2020**, *5*, 9944−9956.
(93) Pavlovich, V. S. Gas-phase energy of the $S_2 \leftarrow S_0$ transition and electrostatic properties of the S_2 state of carotenoid peridinin via a solvatochromic shift and orientation broadening of the absorption spectrum. *Photochem. Photobiol. Sci.* **2014**, *13*, 1444−1455.
(94) Megelski, S.; Lieb, A.; Pauchard, M.; Drechsler, A.; Glaus, S.; Debus, C.; Meixner, A.; Calzaferri, G. Orientation of fluorescent dyes in the nano channels of zeolite L. *J. Phys. Chem. B* **2001**, *105*, 25−35.

https://doi.org/10.1021/acsomega.3c01010
ACS Omega 2023, 8, 15594−15610